Journal of Materials Chemistry C

ROYAL SOCIETY OF CHEMISTRY

PAPER

View Article Online
View Journal | View Issue

Cite this: J. Mater. Chem. C, 2024, 12, 8127

Slow magnetic relaxation and luminescence properties in β-diketonate lanthanide(III) complexes. Preparation of Eu(III) and Yb(III) OLED devices†

Ànnia Tubau,[a] Laura Rodríguez,[a] Piotr Pander,[bcd] Lucy Weatherill,[d] Fernando B. Dias,[d] Mercè Font-Bardía[e] and Ramon Vicente *[a]

The reaction of $[Ln(btfa)_3(H_2O)_2]$ ($btfa^-$ = 4,4,4-trifluoro-1-phenyl-1,3-butanedionate) with 4,4′-dinonyl-2,2′-bipyridyl (4,4′-dinonylbipy) in ethanol allows isolation of mononuclear complexes $[Ln(btfa)_3(4,4'\text{-dinonylbipy})]$ Ln = Sm (**1-Sm**), Eu (**2-Eu**), Tb (**3-Tb**), Dy (**4-Dy**), Er (**5-Er**) and Yb (**6-Yb**). The solid state luminescence emission in the visible region for **1-Sm**, **2-Eu**, **3-Tb** and **4-Dy** and in the NIR region for **1-Sm, 5-Er** and **6-Yb** shows efficient energy transfer from the 4,4,4-trifluoro-1-phenyl-1,3-butanedionate ligands to the central Ln^{3+} ion for all the compounds. Finally, complexes **2-Eu** and **6-Yb** were successfully used as emitters in multilayer vacuum-deposited OLEDs. The electroluminescence quantum efficiency (EQE) of the corresponding devices reached 2.1% and ~0.1–0.2% for **2-Eu** (λ_{EL} = 614 nm) and **6-Yb** (λ_{EL} = 977 nm), respectively. Maximum radiant emittance recorded for the Ln-associated emission achieved 135 μW cm^{-2} for **2-Eu** and 121 μW cm^{-2} for **6-Yb**. These values for efficiency and radiant emittance are unusually high for such type of emitters. Moreover, magnetic studies were performed on all compounds. Alternating current (AC) dynamic measurements indicated Single Molecular Magnet (SMM) behaviour for **4-Dy** and field-induced slow relaxation of the magnetization for complexes **3-Tb**, **5-Er** and **6-Yb**. The anisotropy energy barriers and pre-exponential factors are 91.1 cm^{-1}, τ_0 = 7.2 × 10^{-9} s (under zero magnetic field) and ΔE = 109.3 cm^{-1}, τ_0 = 9.3 × 10^{-10} s under 0.1 T magnetic field for **4-Dy** and ΔE = 24.6 cm^{-1}, τ_0 = 8.7 × 10^{-8} s (under 0.07 T) for **5-Er**. Besides, we observe that for compounds **3-Tb** and **6-Yb** the relaxation of the magnetization does not occur through the Orbach process.

Received 5th March 2024,
Accepted 14th May 2024

DOI: 10.1039/d4tc00902a

rsc.li/materials-c

1. Introduction

Single-molecule magnets (SMMs) refer to magnetically bistable molecules that exhibit slow relaxation of the magnetization below a critical temperature, T_B, while U_{eff} is the energy barrier separating the two spin ground states. By the end of the twentieth century, the effort to obtain SMMs with the highest T_B and U_{eff} focused on transition metal clusters. The first mononuclear lanthanide complexes $([Pc_2Ln]^-\cdot TBA^+$ with Ln = Tb, Dy; Pc^{2-} = phthalocyanine dianion; and TBA^+ = tetrabutylammonium) showing slow relaxation of the magnetization were published in 2003.[1] Consequently, the research effort in the field of SMMs with higher T_B and/or U_{eff} was shifted to complexes derived from lanthanide ions with large orbital momentum and strong magnetic anisotropy.[2] Due to the shielding of the $4f^n$ electrons, the interaction between the lanthanide ion and the donor atoms of the ligands can be considered as electrostatic in nature. Consequently, lanthanide ions have unquenched orbital angular momentum (L) that leads to strong spin–orbit coupling interactions and therefore intrinsic magnetic anisotropy, which make them good candidates for SMMs. Single Ion Magnets (SIMs) are thus mononuclear lanthanide systems that show slow relaxation of the magnetization. A notable example of SIMs are Dy(III)

[a] Departament de Química Inorgànica i Orgànica, Universitat de Barcelona, Martí i Franquès 1-11, E-31321 Barcelona, Spain. E-mail: rvicente@ub.edu
[b] Faculty of Chemistry, Silesian University of Technology, Strzody 9, 44-100 Gliwice, Poland
[c] Centre for Organic and Nanohybrid Electronics, Silesian University of Technology, Konarskiego 22B, 44-100 Gliwice, Poland
[d] Physics Department, Durham University, South Road, Durham, DH1 3LE, UK
[e] Departament de Mineralogia, Cristal·lografia i Dipòsits Minerals and Unitat de Difracció de R-X, Centre Científic i Tecnològic de la Universitat de Barcelona (CCiTUB), Universitat de Barcelona, Solé i Sabarís 1-3, 08028 Barcelona, Spain

† Electronic supplementary information (ESI) available: Thermogravimetric curves, elemental analysis and IR data, SCXRD and PXRD data, excitation spectra, emission spectra at 77 K, ac magnetic data. CCDC 2298951–2298953. For ESI and crystallographic data in CIF or other electronic format see DOI: https://doi.org/10.1039/d4tc00902a

compounds exhibiting an anisotropy barrier, U_{eff}, of 1837 cm^{-1} [3] with T_B = 80 K above that of liquid nitrogen.[4]

In addition to the magnetic properties, the lanthanide(III) ions also display intrinsic photoluminescent properties due to the 4f–4f electronic transitions, which result in long-lived and narrowband photoluminescence. The lanthanide(III) ions have an incompletely filled 4f subshell, which is protected from the coordinating atoms due to the filled $5s^2$ and $5p^6$ orbitals and thus the transitions yield sharp emissive lines characteristics of each central ion. However, the electronic 4f–4f transitions are Laporte forbidden due to the parity selection rule, leading to low molar extinction coefficients ($\varepsilon < 10\ M^{-1}\ cm^{-1}$) for direct photoexcitation of Ln(III) ions. To address this problem, it is necessary to use organic chromophores that absorb energy and subsequently transfer it to the Ln(III) ion. This sensitization mechanism is commonly known as the "antenna effect".[5,6]

The characteristic narrow emission bands and long emission lifetimes of lanthanide(III) coordination compounds over a wide wavelength range (vis/near-IR)[7–14] makes these compounds interesting for potential applications in telecommunications and biological imaging.[15–17] Particular attention has been drawn towards complexes of Nd^{3+}, Er^{3+} and Yb^{3+} cations as they exhibit near infrared (NIR) emission.[6–9,12–14] In this regard, β-diketones are among the most important "antenna ligands" owing to the following merits: (1) they show intense absorption from their conjugated π–π* transitions within a wide wavelength range; (2) they show efficient $S_1 \rightarrow T_1$ intersystem crossing; (3) several β-diketone systems have shown to exhibit optimal triplet state energy, above the emitting level of the lanthanide ion, therefore providing adequate sensitization of the central atom (specially Eu^{3+}); (4) they can form stable adducts with Ln(III) ions through O,O bidentate chelating modes.[18]

The interest in luminescent multifunctional materials that can act as SMMs is increasing.[7,8,19] We have previously published a series of multifunctional Nd(III) coordination complexes[20] derived from the β-diketonate ligand 4,4,4-trifluoro-1-(2-naphthyl)butane-1,3-dionato ($ntfa^-$) of the form $[Nd(ntfa)_3(ANCL)]$, (ANCL = ancillary ligand). More recently we published a new series of luminescent multifunctional SMM materials derived from the 4,4,4-trifluoro-1-phenyl-1,3-butanedionate anion ($btfa^-$) of the form $HAcr[Ln(btfa)_4]$, Ln = Nd(III), Dy(III), and Yb(III); HAcr = acridinium cation, with the aim of studying their photophysical and magnetic behaviour.[21]

To extend the number of multifunctional complexes derived from the β-diketonate anion 4,4,4-trifluoro-1-phenyl-1,3-butanedionate ($btfa^-$), we report here a series of compounds of the form $[Ln(btfa)_3(4,4'\text{-dinonylbipy})]$, Ln = Sm (**1-Sm**), Eu (**2-Eu**), Tb (**3-Tb**), Dy (**4-Dy**), Er (**5-Er**) and Yb (**6-Yb**); 4,4′-dinonylbipy = 4,4′-dinonyl-2,2′-bipyridyl. Alternating current (AC) dynamic measurements of **3-Tb**, **5-Er** and **6-Yb** indicated field-induced slow relaxation of the magnetization under the application of a 0.1, 0.07 and 0.1 T magnetic field, respectively. Besides that, **4-Dy** compound shows SMM behaviour with an anisotropy energy barrier and pre-exponential factor yielding 91.1 cm^{-1} and $\tau_0 = 7.2 \times 10^{-9}$ s respectively. The solid state luminescence in the visible region for **1-Sm**, **2-Eu**, **3-Tb** and **4-Dy** and in the NIR region for **1-Sm**, **4-Dy**, **5-Er** and **6-Yb** upon excitation of ligand-centred absorption bands demonstrate efficient energy transfer from the 4,4,4-trifluoro-1-phenyl-1,3-butanedionate ligands to the central Ln^{3+} ion in all these compounds.

On the other hand, lanthanide(III) complexes show potential as emitters in organic light-emitting diodes (OLEDs). For instance, the Eu^{3+} complexes display high colour purity in red emission. Eu^{3+} complexes provided with an asymmetrical ligand field facilitate the $^5D_0 \rightarrow {}^7F_2$ transition to yield essentially monochromatic single-band red emission at around 612 nm. Similarly, Yb^{3+} complexes displaying photoluminescence at ~1000 nm are ideal candidates for use in NIR OLEDs. Kido *et al.* reported in 1994[22] a ternary Eu^{3+} complex $[Eu(DBM)_3Phen]$ (DBM^- = 1,3-diphenylpropane-1,3-dionate and Phen = 1,10-phenanthroline) showing maximum luminance of 460 cd m^{-2} in an OLED.[23] Since this work β-diketonate ligands have been profusely used in luminescent Ln(III) complexes for application in OLEDs. In this work, we present new OLEDs built by using complexes of the form $[Ln(btfa)_3(4,4'\text{-dinonylbipy})]$, where Ln = Eu(III) in **2-Eu** and Ln = Yb(III) in **6-Yb**. The electroluminescence quantum efficiency (EQE) of the corresponding devices reached 2.1% for **2-Eu** (λ_{EL} = 614 nm) and ~0.1–0.2% for **6-Yb** (λ_{EL} = 977 nm). Maximum radiant emittance recorded for the Ln-associated emission achieved 135 μW cm^{-2} for **2-Eu** and 121 μW cm^{-2} for **6-Yb**. These efficiency and radiant emittance figures are unusually high for such type of emitters.[23]

2. Experimental

2.1. Materials and physicochemical measurements

4,4,4-Trifluoro-1-phenyl-1,3-butanedione and 4,4′-dinonyl-2,2′-bipyridyl were purchased from Sigma-Aldrich. Lanthanide chloride hexahydrates and lanthanide(III) nitrate hexahydrates were obtained from Strem Chemicals. Materials used for OLED fabrication have been purchased from suppliers indicated in parentheses: HAT-CN – dipyrazino[2,3-*f*:2′,3′-*h*]quinoxaline-2,3,6,7,10,11-hexacarbonitrile (sublimed, LUMTEC); TSBPA – 4,4′-(diphenylsilanediyl)bis(*N*,*N*-diphenylaniline) (LUMTEC); mCP – 1,3-bis(carbazol-9-yl)benzene (sublimed, LUMTEC); TPBi – 1,3,5-tris(1-phenyl-1*H*-benzimidazol-2-yl)benzene (Sublimed, LUMTEC); PO-T2T – 2,4,6-tris[3-(diphenylphosphinyl)phenyl]-1,3,5-triazine (LUMTEC); LiF (99.995%, Sigma Aldrich); Al pellets (99.9995%, Lesker).

Infrared spectra (4000–400 cm^{-1}) were recorded in KBr pellets using a PerkinElmer 380-B spectrophotometer. Infrared spectra and a compilation of the most significant bands of all compounds are depicted in Fig. S1 in the ESI.†

The elemental analyses of all compounds were performed at the Serveis Científics i Tecnològics of the Universitat de Barcelona.

2.2. Crystal structure analysis

Crystallographic data for the structures of **2-Eu**, **4-Dy** and **6-Yb** were collected at 100(2) K on a Bruker D8 Venture

diffractometer using Mo-Kα radiation. These data showed that **2-Eu**, **4-Dy** and **6-Yb** were isostructural. Crystallographic data for the structure of **3-Tb** were collected at room temperature (304 K). Crystallographic data of the four complexes are summarized in Table S1 (ESI†). Following data reduction, Lp and absorption corrections (programs APEX and SADABS[24,25] and solution by direct methods, the structures were refined against F^2 with full-matrix least-squares method using the program SHELX-2014).[26] Anisotropic displacement parameters were employed for non-hydrogen atoms. Hydrogen atoms were added at calculated positions and refined by use of a riding model with isotropic displacement parameters based on those of the parent atom. Additional software: Mercury[27] and PLATON.[28] The full crystallographic data for the structures of complexes **2-Eu**, **4-Dy** and **6-Yb** have been deposited at the Cambridge Structural Database (CSD).

Powder X-ray diffraction (PXRD) room temperature measurements were used to verify bulk phase purity. PXRD data were recorded at the Serveis Científics i Tecnològics of the Universitat de Barcelona with *PANalytical X'Pert PRO MPD* θ/θ powder diffractometer of 240 millimetres of radius, in a configuration of convergent beam with a focalizing mirror and a transmission geometry with flat samples sandwiched between low absorbing films Cu Kα radiation (λ = 1.5418 Å). Work power: 45 kV – 40 mA. Incident beam slits defining a beam height of 0.4 millimetres. Incident and diffracted beam 0.02 radians *Soller* slits *PIXcel* detector: Active length = 3.347°. $2\theta/\theta$ scans from 2 to 70° 2θ with a step size of 0.026° 2θ and a measuring time of 298 seconds per step. The alert found in structures **4-Dy** and **6-Yb** were mainly due to the fact that there is a q peak that is not assigned to any element. However, when observed closely the electron density appears close to the lanthanide ion. For **4-Dy** the more intense q peaks appear at a distance of 0.970 and of 0.996 Å from the Dy^{3+} ion. For **6-Yb** the more intense q peak appear at a distance of 1.75 Å from the last sp^3 C atom of one of the aliphatic chains. Hence, due to the inconsistent distance, it is unlikely that such residual density originates form unaccounted atom types since this residual density peak challenges any chemical interpretation. Moreover, powder X-ray diffraction analysis matches the pattern calculated from both single crystal structures. This alert probably arises from strong absorption effects that could not be fully corrected.

2.3. Magnetic measurements

Magnetic measurements were performed by the Mesures Magnètiques Unit from Scientific and Technological Centers (CCiTUB), Universitat de Barcelona, using a Quantum Design MPMS-XL SQUID magnetometer. Pascal's constants were used to estimate the diamagnetic corrections, which were subtracted from the experimental susceptibilities to give the corrected molar magnetic susceptibilities.

2.4. Thermogravimetric measurements

Thermogravimetric analysis (TGA) measurements were carried out under N_2 atmosphere in a Mettler TG 50 instrument at a heating rate of 10 °C min^{-1}. For compounds **2-Eu** and **6-Yb**, TGA measurement were performed in the temperature range between 30 and 600 °C. The sample weight stays steady up until 250–300 °C where it loses 75.2% of its weight. Decomposition of the compounds is observed at temperatures above 300 °C (Fig. S2, ESI†).

2.5. Luminescence measurements

Solid state and solution fluorescence spectra were recorded on a Horiva Jobin Yvon SPEX Nanolog fluorescence spectrophotometer equipped with a three slit double grating excitation and emission monochromator with dispersions of 2.1 nm mm^{-1} (1200 grooves per mm) at room temperature. The steady-state luminescence was excited by unpolarized light from a 450 W xenon CW lamp and detected at an angle of 22° for solid state and of 90° for the solution measurements by a red-sensitive Hamamatsu R928 photomultiplier tube. Spectra were reference corrected for both the excitation source light intensity variation (lamp and grating) and the emission spectral response (detector and grating). Near infra-red spectra were recorded at an angle of 22° using a liquid nitrogen cooled, solid indium/gallium/arsenic detector (850–1600 nm). To measure the emission spectra, samples were excited at the excitation wavelength (λ_{exc}) of 306 nm for **1-Sm** and **2-Eu**, of 320 nm for **3-Tb** and of 360 nm for **6-Yb**, for solution samples. Solution samples **4-Dy** and **5-Er** were excited at the emission wavelength of 320 nm according to the absorption spectra since no reliably excitation spectra could be obtained. Polycrystalline samples were excited at the λ_{exc} of 359 nm for **1-Sm** to **6-Yb**.

The excited state decay curves were measured in the same instrument in the phosphorescence mode using a 450 W xenon pulsed lamp (1.5 ns pulse). Experiments were monitored at the respective λ_{exc} and at the emission wavelength (λ_{em}) of 651 nm ($^4G_{5/2} \rightarrow {}^6H_{9/2}$) for **1-Sm** and of 614 nm ($^5D_0 \rightarrow {}^7F_2$) for **2-Eu**. The measured decays were analyzed using the Origin software package. Both decay curves fitted monoexponentially: $\ln(I) = \ln(I_0) - \frac{1}{\tau_{obs}}$. The fit quality was determined by Pearson's χ^2 test. Luminescence quantum yields (ϕ^L_{Ln}) were recorded using an Absolute PL quantum yield spectrometer from Hamamatsu Photonics upon excitation of samples at the respective λ_{exc}.

2.6. OLED characterization

We used pre-cleaned indium-tin-oxide (ITO) coated glass substrates with a sheet resistance of 20 Ω sq^{-1} and ITO thickness of 100 nm. The substrates were first washed with distilled water, acetone and then sonicated in acetone and isopropanol, for 15 min each time. Substrates were dried with compressed air and transferred into an oxygen plasma generator for 6 min at full power. Thermally deposited layers were obtained using Kurt J. Lesker Spectros II deposition system at 10^{-6} mbar base pressure. All organic materials and aluminium were deposited at a rate of 1 Å s^{-1}. The LiF layer was deposited at a rate of 0.1–0.2 Å s^{-1}. Characterisation of OLED devices was conducted in a 10 inch integrating sphere (Labsphere) connected to a Source Measure Unit (SMU, Keithley) and coupled with a spectrometer

USB4000 or QePro (Ocean Optics). Further details are available in reference.29 Devices of 4 × 2 mm pixel size were fabricated.

2.7. Syntheses of the complexes

Synthesis of [Ln(Btfa)$_3$(H$_2$O)$_2$]. A methanol solution (10 mL) containing NaOH (6 mmol, 240 mg), HBtfa (6 mmol, 1296.9 mg) and $LnCl_3{\cdot}nH_2O$ (2 mmol) was stirred for 1 hour at room temperature. Then 80 mL of deionized water were added to the reaction mixture and it was allowed to stir overnight. The pale precipitate (light pink for the Er^{3+} compound) was filtrated and dried under vacuum (yield: 70–80%).[21]

Synthesis of [Ln(Btfa)$_3$(4,4′-dinonyl-2,2′-bipy)]. An ethanol solution (15 mL) containing 4,4′-dinonyl-2,2′-bipy (1 mmol, 408.7 mg) was added to another ethanol solution (15 mL) containing the corresponding [Ln(Btfa)$_3$(H$_2$O)$_2$] (1 mmol). The solution was stirred for 30 minutes and then left to stand at room temperature. Block like single crystals suitable for X-ray diffraction were obtained within a week (yield: 60–70%).

3. Structural characterization

3.1. Monocrystalline X-ray diffraction

Addition of the 4,4′-dinonyl-2,2′-bipyridyl ligand to the [Ln(Btfa)$_3$(H$_2$O)$_2$] precursor, yielded neutral mononuclear compounds with formula [Ln(Btfa)$_3$(4,4′-dinonyl-2,2′-bipy)]: Ln = Sm^{3+}(**1-Sm**), Eu^{3+} (**2-Eu**), Tb^{3+} (**3-Tb**), Dy^{3+} (**4-Dy**), Er^{3+} (**5-Er**) and Yb^{3+} (**6-Yb**). The single crystal X-ray diffraction structure at 100 K was obtained for compounds **2-Eu**, **4-Dy** and **6-Yb**. Crystallographic details from the measurement and selected bond distances and angles are compiled in Tables S1 and S2 (ESI†) respectively. Compounds **1-Sm** to **6-Yb** are isostructural, therefore only the structure of compound **2-Eu** will be described, Fig. 1(left).

Compound **2-Eu** crystallizes in a triclinic crystal system and a P$\bar{1}$ space group. The Eu^{3+} metal ion is octacoordinated and the EuO_6N_2 polyhedron is made up of six O atoms from three β-diketonate ligands with Eu–O bond distances in the range of 2.343–2.389 Å and two N atoms from one polypyridyl ancillary ligand with Eu–N distances of 2.559 and 2.575 Å. The closest Eu···Eu intermolecular distance is 8.968 Å. The six oxygen and two nitrogen atoms are gathered around the Eu^{3+} central ion, forming a geometrical polyhedron that is close to an ideal square antiprism (SAPR-8, D_{4d} symmetry) Fig. 1(right). One of the basal planes is made up of the O1, O2, N1 and N2 atoms and the other one of O3, O4, O5 and O6. The geometry has been calculated with the SHAPE program.[30,31] For compound **2-Eu** the deviation from the optimal polyhedron accounted by the continuous shape measurement (CShM) values for the SAPR-8 geometry is 1.040. For compounds **4-Dy** and **6-Yb** the CShM values for the SAPR-8 geometry are 0.902 and 0.790 respectively.

The crystal packing in **2-Eu** is built up through weak intermolecular interactions. Fig. S3 (ESI†) therefore, we can consider that the mononuclear complexes are isolated one from the other through the crystal lattice.

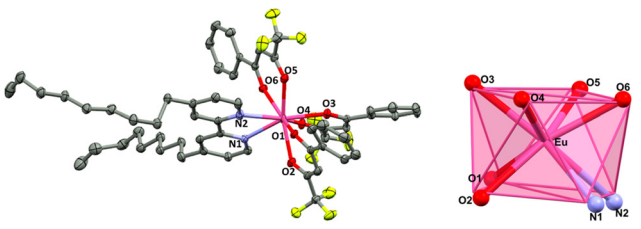

Fig. 1 Left: Crystal structure of complex **2-Eu** with labels for atoms coordinating the central ion. Hydrogen atoms have been omitted for clarity. Right: Ideal coordination polyhedron superimposed on the coordination sphere around the Eu^{3+} ion.

3.2. Powder X-ray diffraction

To verify the crystallinity and phase purity in bulk, Powder X-ray Diffraction (PXRD) were recorded at room temperature for **1-Sm** to **6-Yb** complexes. The measured PXRD were compared to the calculated pattern obtained from the single crystal structure of **2-Eu**, **4-Dy** and **6-Yb** recorded at 100 K, Fig. S4 (ESI†). Interestingly, we observed that the experimental and calculated patterns did not match. Therefore, we then perform a single crystal measurement at room temperature (304 K) using **3-Tb** crystals (Fig. S5 and Table S1, ESI†). The calculated powder pattern obtained from this measurement matches the powder diffractograms of the other complexes, Fig. S6 (ESI†). From these results we conclude that upon changing the temperature from 300 K to 100 K, there is a slight change in the atomic coordinates of the crystals which results in a noticeable difference in some cell parameters (*i.e.* parameter b is greater compared to the 100 K measurements), thus leading to a different PXRD pattern, but the crystal cell and space group remain the same, Table S1 (ESI†).

4. Optical properties

Absorption spectra were recorded for all complexes in chloroform solutions ($c = 10^{-6}$ M), Fig. 2a. Spectra of complexes **1-Sm** to **6-Yb** show similar absorption pattern in the 235–370 nm range. As a means of assigning the absorption bands shown by the coordination complexes, absorption spectra were also recorded for the free ligands separately. The 4,4′-dinonyl-2,2′-bipy ligand was diluted in chloroform solution ($c = 10^{-6}$ M) and HBtfa was diluted in a 1 mM NaOH chloroform solution to measure absorption of respective β-diketone salt, Fig. 2b. Absorption spectrum of the free 4,4′-dinonyl-2,2′-bipy show two bands at 242 and 282 nm while Btfa shows an intense band at 325 nm and less intense bands at 220–248 nm corresponding to the π → π* and n → π* singlet state transitions. The UV-Vis absorption spectra of **1-Sm** to **6-Yb** correlate with those of the constituent ligands. The band corresponding to coordinated Btfa absorption appears slightly blue shifted, compared to the free ligand, about 6 nm. Whereas the absorption bands of 4,4′-dinonyl-2,2′-bipy where red-shifted, compared to the free ligand, about 25 nm nm upon coordination. The band appearing at 282 nm in the free 4,4′-dinonyl-2,2′-bipy spectra appears as a shoulder around 310 nm in the complexes spectra

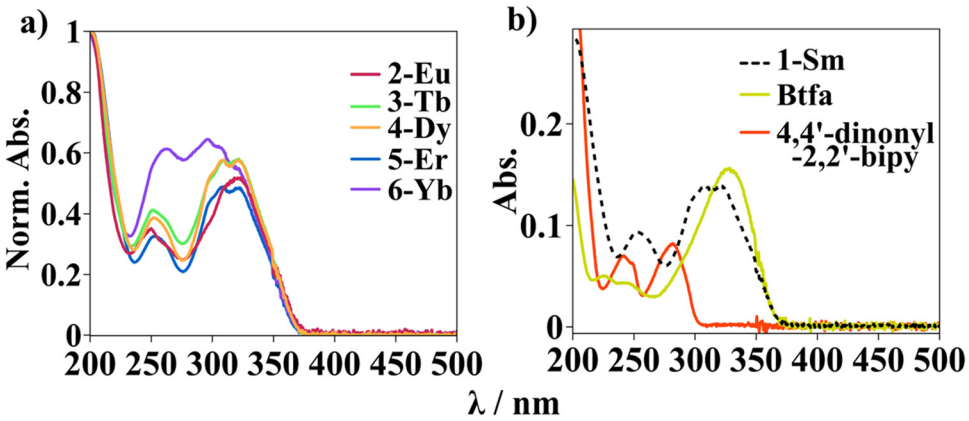

Fig. 2 Absorption spectra of (a) the Ln^{3+} compounds in chloroform solutions $c = 10^{-6}$ M; and (b) spectra of the free 4,4′-dinonyl-2,2′-bipy ligand in $CHCl_3$ solution and spectra of Btfa salt in a 1 mM NaOH, $CHCl_3$ solution. The free ligand absorption spectra has been superimposed onto **1-Sm** spectra for sake of wavelength shift comparison.

superimposing to the Btfa associated absorption band. This may explain the intense and broader band appearing at 277–370 nm. Similar UV-Vis absorption spectra are obtained for previous published [Ln(β-diketonate)$_3$(L)] systems, where L is the ancillary ligand based on *N*,*N*-donor polypyridyl molecules.[18g,h]

The emission spectra of all complexes in the series **1-Sm** to **6-Yb** were recorded in $CHCl_3$ solutions and in polycrystalline samples. The measurements were monitored by exciting the samples at the respective absorption maxima (Fig. 2(left) and Fig. S7, ESI†) giving rise to the emission of the respective lanthanide f–f transitions in the visible (400–700 nm) and NIR range (800–1600 nm) (Fig. 3). The expected emission profiles are recorded in all cases (with slightly better resolution in the polycrystalline samples) except for **4-Dy** and **6-Er** where no significant emission was observed in solution. Emission bands displayed by the aforementioned lanthanide compounds are assigned in Fig. 3 and a compilation of the obtained wavelengths with the assignation of each transition can be found in Table S3 (ESI†). The characteristic red, green, and yellowish photoluminescence emission color of the **1-Sm**, **2-Eu**, **3-Tb** and **4-Dy** samples in solid state and in solution, were sufficiently intense to be observed with the naked eye, Figs. S8 and S9 (ESI†). Color coordinates were calculated for all emission spectra recorded in solid and solution state and are shown in the CIE chromaticity diagram 1931 in Fig. S10 (ESI†).

The characteristic emission originated from the f–f transitions of each lanthanide ion can be observed for **1-Sm**, **2-Eu**, **3-Tb**, and **5-Yb** with no residual emission of the ligand in the 300–500 nm range. This indicates an efficient energy transfer from the excited state of the ligand to the lanthanide emitting energy levels, the so-called antenna effect. This is also confirmed by the corresponding excitation spectra which shows the broad and intense band corresponding to the ligand while excitation transitions corresponding to the f–f lanthanide(III) ions are not observed.[32] The emission bands at 564, 608, 647 and 707 nm found in the **1-Sm** spectrum are assigned to the transitions from the $^4G_{5/2}$ energy level to the $^6H_{5/2}$, $^6H_{7/2}$, $^6H_{9/2}$ and $^6H_{11/2}$ levels of the ^6H_J ground state respectively, Fig. 3a. Additional bands are found in the NIR range, at 953 nm assigned to the $^4G_{5/2} \rightarrow {}^6F_{5/2}$ transition overlapped with the $^4G_{5/2} \rightarrow {}^6F_{1/2}$, $^4G_{5/2} \rightarrow {}^6H_{15/2}$ and $^4G_{5/2} \rightarrow {}^6F_{3/2}$ transitions. The less intense bands found at 1033, 1188 and 1300 nm are assigned to $^4G_{5/2} \rightarrow {}^6F_{7/2}$, $^4G_{5/2} \rightarrow {}^6F_{9/2}$ and $^4G_{5/2} \rightarrow {}^6F_{11/2}$ transitions respectively. A better defined NIR emission spectrum was observed for **1-Sm** polycrystalline sample than in $CHCl_3$ solution.

The emission spectrum of **2-Eu** displays several bands at 579, 592 and 611 nm (most intense) that are assigned to the $^5D_0 \rightarrow {}^7F_0$ ($\Delta J = 0$), $^5D_0 \rightarrow {}^7F_1$ (split due to the crystal field) and $^5D_0 \rightarrow {}^7F_2$ transitions respectively, Fig. 3b. While the band at 592 nm is a pure magnetic dipole transition in which the intensity is practically independent of the Eu^{3+} environment, the signal at 611 nm is assigned to the hypersensitive band since it accounts for an electric dipole transition. From the latter, the structure of the band is distinguished where at least three components, ascribed to the $^5D_0 \rightarrow {}^7F_2$ transition, can be discerned. Differentiation of $^5D_0 \rightarrow {}^7F_2$ components may indicate that the Eu^{3+} ion is not occupying an inversion symmetry site inside the structure which agrees with the coordination geometry obtained from the SHAPE calculations (square antiprism, D_{4d} symmetry). The less intense bands at 651 and at 703 nm are assigned to $^5D_0 \rightarrow {}^7F_3$ and $^5D_0 \rightarrow {}^7F_4$ transitions, respectively.

For compound **3-Tb**, the bands found at 489, 545, 581 and 619 nm are assigned to the transitions from the $^5D_4$ emissive state to the ground state $^7F_6$, $^7F_5$, $^7F_4$ and $^7F_3$ energy levels, respectively. As for **4-Dy**, emission of the $CHCl_3$ solution, is mainly dominated by the ligand in the 300–400 nm range instead of the transitions centered at the Dy^{3+} ion. While for the polycrystalline sample, three intense emission bands originating from the dysprosium(III) $^7F_{9/2}$ emissive energy level are differentiated at 481, 577, and 664 nm, Fig. 3d. The bands are assigned to $^7F_{9/2} \rightarrow {}^6H_{15/2}$, $^7F_{9/2} \rightarrow {}^6H_{13/2}$ and $^7F_{9/2} \rightarrow {}^6H_{11/2}$ transitions, respectively. In addition, a very low intense signal at 454 nm is observed. This signal is assigned to the forbidden

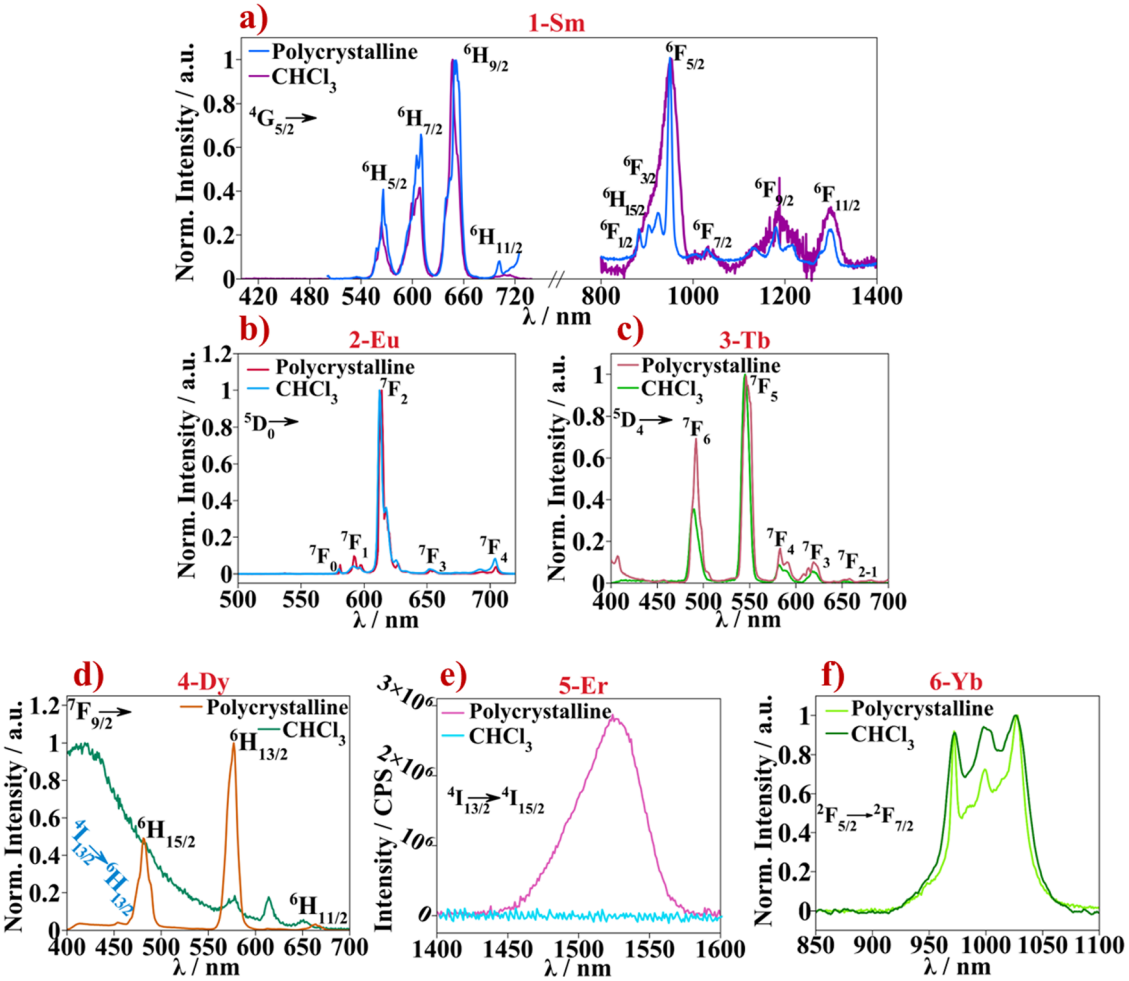

Fig. 3 Luminescence emission spectra of compounds **1-Sm** to **6-Yb** measured in polycrystalline samples and in a $1{\cdot}10^{-6}$ M $CHCl_3$ solution. To measure the emission spectra, samples were excited at the excitation wavelength (λ_{exc}) of 306 nm for **1-Sm** and **2-Eu**, 320 nm for **3-Tb** and 360 nm for **6-Yb**, for solution samples. Moreover, solution samples of **4-Dy** and **5-Er** were excited at the emission wavelength of 320 nm according to the absorption profile since no reliably excitation spectra could be obtained. Polycrystalline samples were excited at the λ_{exc} of 359 nm for **1-Sm** to **6-Yb**.

magnetic dipole transition ($\Delta J = 0$) $^4I_{13/2} \rightarrow {}^6H_{13/2}$, such as in the case of $^5D_0 \rightarrow {}^7F_0$ in the Eu^{3+} ion.[33] Furthermore, for the NIR Er^{3+} emitter (**5-Er**), emission is totally quenched when the compound is found in the $CHCl_3$ solution. However, in the solid-state sample, Er^{3+} centered emission is observed at 1526 nm which is assigned to the $^4I_{13/2} \rightarrow {}^4I_{15/2}$ transition, Fig. 3e. Finally, sample **6-Yb** displays the expected Yb^{3+} band corresponding to the $^5F_{5/2} \rightarrow {}^2F_{7/2}$ transition appearing at 1000 nm, Fig. 3f. The band splitting due to crystal field effects is clearly visible.[32,34]

Emission spectra of the polycrystalline samples were also recorded at 77 K (Fig. S11, ESI†). Under these conditions, the crystal field splitting of the emission bands acquires better resolution in all the polycrystalline samples except for the **5-Er** compound (not shown) where the emission spectrum remains unchanged from the luminescence observed at room temperature. For compounds **1-Sm**, **4-Dy** and **6-Yb** the splitting into $J + \frac{1}{2}$ component (for Kramer ions) due to crystal field can be clearly observed. However, for compounds **2-Eu** and **3-Tb**, the $2J + 1$ (non-Kramer ions) splitting of each emission band is not clearly resolved. Perhaps even lower temperatures than 77 K are necessary to obtain high-resolution spectra in this case.[32]

Interestingly, the NIR spectra of the **4-Dy** compound, for which emission has not been observed at room temperature, could be recorded at 77 K, Fig. S11e (ESI†). Clear bands are now discerned at 964 and 1154 nm which are assigned to the $^4F_{9/2} \rightarrow {}^6F_{7/2}$ and $^4F_{9/2} \rightarrow {}^6F_{5/2}$ f–f Dy^{3+} transitions, respectively. Furthermore, the third band found at 1018 nm is attributed to the $^6H_{5/2} + {}^6F_{7/2} \rightarrow {}^6H_{15/2}$ transition.[35]

4.1. Photoluminescence quantum yield (ϕ^L_{Ln}) and luminescence decay time (τ_{obs})

The overall photoluminescence quantum yields (ϕ^L_{Ln}) and luminescence decay times (τ_{obs}) were measured in both, $CHCl_3$ solution and polycrystalline samples at room temperature, and the results are presented in Table 1.

2-Eu is the complex showing the highest ϕ^L_{Ln} and longest luminescence lifetime that is at least one order of magnitude

Table 1 Overall quantum yields and luminescence lifetime of compounds **1-Sm** to **4-Dy** measured in polycrystalline samples ($\phi^{L}_{Ln\ polycryst}$ and $\tau_{obs\ polycryst}$) and $CHCl_3$ solutions ($\phi^{L}_{Ln\ solution}$ and $\tau_{obs\ solution}$). Samples were excited at the respective absorption maxima (see Section 2.7 of the Experimental section)

	$\phi^{L}_{Ln\ polycryst}$	$\phi^{L}_{Ln\ solution}$	$\tau_{obs\ polycryst}$ (ms)	$\tau_{obs\ solution}$ (ms)
1-Sm	0.03	0.03	0.06	0.07
2-Eu	0.68	0.42	0.90	0.65
3-Tb	0.01	0.006	[a]	[a]
4-Dy	0.005	[a]	[a]	[a]

[a] Value not recorded due to limitations in the equipment.

larger compared to the values recorded for the other compounds. The ϕ^{L}_{Ln}values recorded for **2-Eu**, **3-Tb** and **4-Dy** are about 2-fold higher in the polycrystalline samples than in chloroform solution. Lifetimes are in order of ~60–70 μs (**1-Sm**) to ~1 ms (**2-Eu**) while all samples display monoexponential luminescence decay (Fig. 4). The presence of a single decay time component, τ_{obs}, for **1-Sm** and **2-Eu** is suggestive of a single radiative deactivation process, both in the solid state and in solution.[34]

The low ϕ^{L}_{Ln} values observed in **3-Tb** are consistent with other reported in the literature. For these compounds, low luminescence ϕ^{L}_{Ln} are related to back energy transfer due to the low energy gap between the lowest triplet state of the ligands and terbium(III) $^5D_4$ (20 400 cm^{-1}) emitting energy level. Latva *et al.*[36] concluded that the back transfer energy (studied for a large group of Tb^{3+} coordination compounds) usually occurred when this energy difference was below 1850 cm^{-1}. In this regard, the gadolinium analogue of compounds **1-Sm** to **6-Yb**, [Gd(Btfa)$_3$(4,4′-dinonyl-2,2′-bipy)] **7-Gd**, was synthetized. From the edge of the UV absorption spectrum the singlet state (S_1) energy was obtained, 27 137 cm^{-1} (376 nm), Fig. S12 (ESI†) bottom left. The triplet state energy can be deduced from the 0-phonon band of the Gd^{3+} analogue phosphorescence spectrum measured at 77 K which appeared at 21 229 cm^{-1} (471 nm), Fig. S12 (ESI†) bottom right. The energy separating the S_1 and T_1 state is 5908 cm^{-1}. Such small singlet–triplet energy difference (below 7000 cm^{-1}) favors intersystem crossing ($S_1 \rightarrow T_1$) leaving behind other competitive processes such as relaxation back to the S_0 ground state.[37a] Moreover, the energy difference between the lowest triplet state and the emissive Tb^{3+} energy level, is 829 cm^{-1}. Thus, following Latva's rule, compound **3-Tb** shows a low quantum yield due to back energy transfer taking place as a result of the low energy difference between T_1 and terbium's $^5D_4$ emitting level.[37]

Additionally, the narrow energy gap of the Sm(III) cation promotes nonradiative relaxation processes, shortening luminescence decay and reducing luminescence efficiency. This also explains the low values of ϕ^{L}_{Ln} and τ_{obs} obtained for **1-Sm** which are common in other Sm-β-diketone systems.[38] For **5-Yb** and **6-Er** samples, the QY could not be measured as being too low to be recorded accurately.

Additional parameters regarding the sensitization mechanism of **2-Eu** system can be calculated. Owing to the pure magnetic dipole character of $^5D_0 \rightarrow {}^7F_1$ transition, the radiative lifetime (τ_{rad}) from the $^5D_0$ emissive level, of **2-Eu** compound can be calculated from the corrected emission spectrum, eqn (S2) (ESI†).[39] For the Eu^{3+} polycrystalline sample τ_{rad} is 1.26 ms and 1.23 ms for the $CHCl_3$ solution. Then the intrinsic quantum yield (ϕ^{L}_{Ln}) is 0.71 and 0.53 for the solid and solution samples, respectively (see Section 1.3 of ESI†). Moreover, the amount of energy absorbed by the chromophore ligands that is transferred to the excited state of the lanthanide ion is known as the sensitization efficiency (η_{sens}), and it plays a significant role in the overall quantum yield, which is defined as: $\phi^{L}_{Ln} = \eta_{sens} \cdot \phi^{Ln}_{Ln}$. Thus, the η_{sens} figures of 0.95 in polycrystalline powder and of 0.79 in $CHCl_3$ solution, show a nearly 100% efficient sensitization of the [Eu$_2$(Btfa)$_3$(4,4′-dinonyl-2,2′-bipy)] (**2-Eu**) system in solid state.[34,37a]

4.2. Stability of the coordination sphere in $CHCl_3$ solutions

If the corresponding normalized emission profiles in $CHCl_3$ and polycrystalline samples are superimposed and observable changes are differentiated, a change in the lanthanide coordination environment due to solvation effects may be considered and therefore a lack of stability in solution of the coordination compound. However, emission spectra of the aforementioned

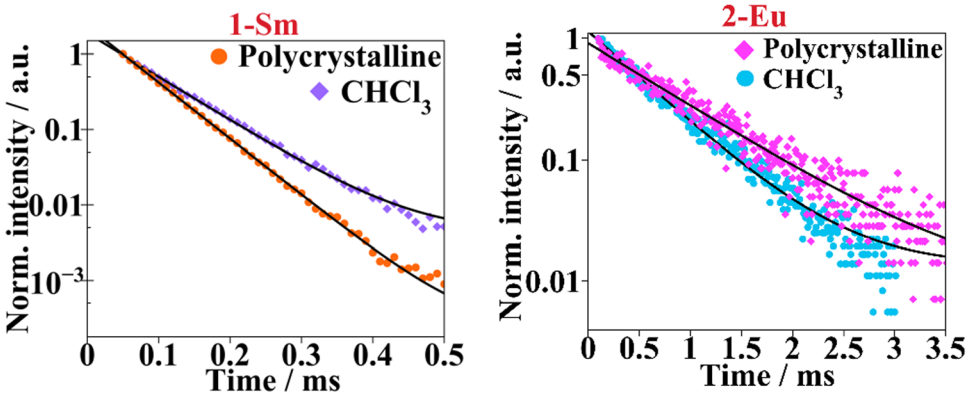

Fig. 4 Luminescence lifetime curves are presented in semi-log plots for complexes **1-Sm** and **2-Eu**. The solid black lines represent the mono-exponential fitting with $I(t) = I_0 e^{-\frac{t}{\tau_{obs}}} + C$.

compounds have similar shape, hinting that the coordination compound are still present in the $CHCl_3$ solution.

Moreover, spectroscopic–structure correlation (from solid state and $CHCl_3$ solution) can be derived from the corrected emission spectra of **1-Sm** and **2-Eu** compounds owing to the distinctive emission bands exhibited by these lanthanide ions. The crystal field splitting of the hypersensitive band ($^5D_0 \rightarrow {}^7F_2$) recorded for Eu^{3+} compound is the same in both solid and solution. Also, the integrated area of the magnetic dipole transition ($^5D_0 \rightarrow {}^7F_1$) to the electric dipole ratio ($0 \rightarrow 1/0 \rightarrow 2$) gives information about the asymmetry factor being 0.09 for the polycrystalline sample and 0.07 in chloroform. The ratio between these two bands is minor, evidencing that there is no significant change around the Eu^{3+} environment when dissolving the **2-Eu** sample into chloroform. Same reasoning can be done for the **1-Sm** compound since $^4G_{5/2} \rightarrow {}^6H_{9/2}$ transition also has a hypersensitive character (yet not as strong as in Eu^{3+}) and $^4G_{5/2} \rightarrow {}^6H_{5/2}$ is predominantly magnetic dipole in nature. Then for the polycrystalline sample the $(5/2 \rightarrow 5/2)/(5/2 \rightarrow 9/2)$ ratio is 0.26 and for the $CHCl_3$ is 0.22. The difference of the asymmetric factor of **1-Sm** is similar on changing the phase from solid to solution as well, therefore, suggesting that structural changes in the samarium(III) environment are the slightest due to solvating effects.[34,38a]

By comparing the QY and η_{sens} values for the polycrystalline and solution samples we reach similar conclusions. Both diminish on dissolving the samples in $CHCl_3$. There are more degrees of freedom in solution media (*i.e.* vibrations and rotations), hence escalating the non-radiative decay. In this way, **4-Dy** and **5-Er** solution samples are virtually non-emissive.

4.3. Organic light-emitting diodes (OLEDs)

Despite their large molecular weight, complexes **2-Eu** and **6-Yb** sublime at relatively low temperatures, around 140–150 °C (significantly below the decomposition temperature at ~290 °C) at ~10^{-6} mbar pressure. This may be due to their ball-like geometry and the peripheral alkyl and $-CF_3$ ligand groups that reduce intermolecular interactions and increase the volatility of the material. This type of design is highly desirable in materials used in the emissive layer of OLEDs. Vacuum-deposited devices were produced as a proof-of-concept with this group of luminescent materials. OLED electroluminescence and electrical characteristics are shown in Fig. 5 and Fig. S13–S15 (ESI†) as well as in Table 2.

The complex **2-Eu** displays high photoluminescence quantum yield (PLQY) both in neat film and in powder, indicating that photoluminescence quenching is negligible in the solid state. As **2-Eu** can be used at higher loads in the emissive layer, OLEDs incorporating **2-Eu** at 20% load in the hole-transporting host mCP were produced {**Device 1**: ITO|HAT-CN (10 nm)|TSBPA (40 nm)|mCP (2 nm)|mCP co 20% **2-Eu** (20 nm)|PO-T2T (5 nm)|TPBi (40 nm)|LiF (0.8 nm)|Al (100 nm)} or in the blend host mCP : TPBi {**Device 2**: ITO|HAT-CN (10 nm)|TSBPA (40 nm)|mCP (2 nm)|mCP : TPBi (60 : 40) co 20% **2-Eu** (20 nm)|TPBi (50 nm)|LiF (0.8 nm)|Al (100 nm)}. As **2-Eu** does not significantly absorb light above 400 nm and its absorbance in the 350–400 nm region is limited, a non-negligible level of host luminescence contaminating the EL spectrum is observed. An alternative approach to **Devices 1** and **2** was to use a 5 nm thick neat emissive layer of **2-Eu** sandwiched between electron-blocking and hole-blocking materials {**Device 3**: ITO|HAT-CN (10 nm)|TSBPA (40 nm)|**2-Eu** (5 nm)|PO-T2T (20 nm)|TPBi (30 nm)|LiF (0.8 nm)|Al (100 nm)}. This strategy led to the host emission being eliminated and colour purity improved. However, the maximum luminance of this OLED was significantly reduced.

All three OLED structures (OLEDs **1**–**3**) display similar EL spectra typical of luminescence originating from Eu^{3+} complexes with visibly narrowband emission peak at 614 nm. Significantly less intense emission bands in the region 530–710 nm are also observed. These EL spectra are significantly narrowband with FWHM of 6–8 nm leading to high colour purity, with potential for good colour rendering in displays. The modest maximum external quantum efficiency (EQE) of 2.0–2.1% and luminance ~200–600 cd m^{-2} is most likely a result of

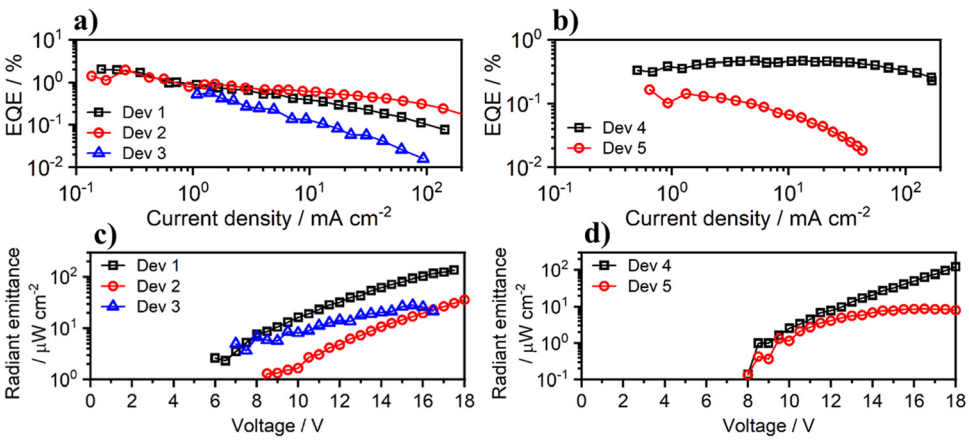

Fig. 5 External quantum efficiency (EQE) *vs.* current density characteristics of devices **1**–**5** from compounds (a) **1-Eu** and (b) **6-Yb**. Radiant emittance *vs.* voltage bias for devices **1**–**5** from compounds (c) **1-Eu** and (d) **6-Yb**.

Table 2 Electroluminescent properties of OLED devices **1–5**

	Dev 1	Dev 2	Dev 3	Dev 4	Dev 5
Emitter	**2-Eu**	**2-Eu**	**2-Eu**	**6-Yb**	**6-Yb**
V_{ON}/V^a	4.5	5.0	4.0	4.0	4.5
L_{max}/cd m^b	210	590	20	477	4
R_{max}/μW cm^c	135^h	36^h	28^h	121^i	9^i
λ_{EL}/nm^d	581, 593, 614, 655, 694, 704^h	581, 593, 614, 655, 694, 704^h	581, 593, 614, 655, 694, 704^h	977, 1005, 1031^i	977, 1005, 1031^i
CIE 1931 (x; y)^e	(0.51; 0.30)	(0.52; 0.28)	(0.60; 0.30)	—	—
CE_{max}/cd A^f	2.6	2.6	0.4	—	—
EQE_{max}/%^{g}	2.1	2.0	0.6	0.46/0.10^i	0.17

^{a} Turn-on voltage at 10^{-2} mA cm^{-2}. ^{b} Maximum luminance (visible spectrum). ^{c} Maximum radiant emittance for the EL bands associated with the emitter. ^{d} EL maxima associated with the emitter emission. ^{e} Colour coordinates of electroluminescence spectrum in colour space CIE 1931 as defined by the International Commission on Illumination. ^{f} Maximum current efficiency. ^{g} Maximum external quantum efficiency. ^{h} For wavelength range $\lambda > 550$ nm. ^{i} For wavelength range $\lambda > 900$ nm.

the long photoluminescence lifetime characteristic of Eu^{3+}complexes.

Similarly to **2-Eu**, complex **6-Yb** also offers attractive luminescent properties, but this time in the near infra-red region. OLEDs with the similar structure of **Device 2** but using **6-Yb** as the emitter were produced (**Device 4**). A significant electroluminescence contribution from the host material is visible in this device, mostly due to the relatively small PLQY of the **6-Yb** complex. However, the electroluminescence originating from the **6-Yb** emitter appears at relatively longer wavelengths in the near infra-red region, and hence is attractive for various potential practical applications. The ~1000 nm electroluminescence band on its own reaches a maximum radiant emittance of 121 μW cm^{-2} and 0.1% EQE, which is comparable with other emitters in this wavelength range. In order to eliminate the electroluminescence from the host material, we used complex **6-Yb** in neat film, reproducing the structure of **Device 3**. However, the thickness of 5 nm was found to be insufficient and a significant electroluminescence from a through-space TSBPA:PO-T2T exciplex was observed. Hence, **Device 5** features an emissive layer of 10 nm **6-Yb** neat film. This device produces a relatively strong near infra-red electroluminescence at ~1000 nm, but a weak contribution from the TSBPA:PO-T2T exciplex is still present.

Magnetic properties

DC measurements. Direct current (DC) magnetic susceptibility (χ_M) and magnetization (M) measurements were performed on polycrystalline samples **1-Sm** to **6-Yb**. The χ_M measurements were carried out under a DC field of 0.3 T in the 2–300 K temperature range. The temperature dependence of $\chi_M T$ is shown in Fig. 6. $\chi_M T$ values at room temperature (300 K) are 0, 1.3, 11.8, 15.0, 11.2 and 2.6 cm^3 mol^{-1} K for **1-Sm**, **2-Eu**, **3-Tb**, **4-Dy**, **5-Er**, and **6-Yb** respectively. For one isolated Ln^{3+} cation, the calculated $\chi_M T$ values are: 0.09 cm^3 mol^{-1} K for Sm^{3+} ground state $^6H_{5/2}$ and g_j = 2/7; 0 cm^3 mol^{-1} K for Eu^{3+} ground state $^7F_0$; 11.82 cm^3 mol^{-1} K for Tb^{3+} ground state $^7F_6$ and g_j = 3/2; 14.17 cm^3 mol^{-1} K for Dy^{3+} ground state $^6H_{15/2}$ and g_j = 4/3, 11.48 cm^3 mol^{-1} K for Er^{3+} ground state $^4I_{15/2}$ and 2.57 cm^3 mol^{-1} K for Yb^{3+} ground state $^2F_{7/2}$ and g_j = 8.7.[32a]

Owing to the relatively small spin–orbit coupling parameter (λ) splitting the ^6H_J (for Sm^{3+}) and ^7F_J (for Eu^{3+}) states, the J states higher in energy are found to be electronically populated at room temperature. This may explain why room temperature $\chi_M T$ values of **1-Sm** and **2-Eu** determined experimentally are larger than the calculated values. Upon cooling both samples, $\chi_M T$ curves decrease due to thermal depopulation of the excited J states of Sm^{3+} and Eu^{3+} ions respectively.[40]

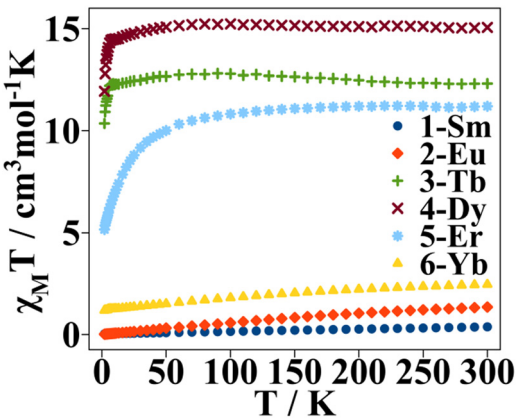

Fig. 6 Temperature dependence of $\chi_M T$ measured at an external static field of 0.3 T, for compounds **1-Sm** to **6-Yb**.

Room temperature $\chi_M T$ of **3-Tb**, **4-Dy**, **5-Er** and **6-Yb** agree with the calculated parameters for an isolated Ln^{3+} ion. Upon decreasing the temperature, the $\chi_M T$ curves of the four compounds remain nearly constant until ~50 K. Below this temperature, $\chi_M T$ values decrease suddenly to 10.3, 11.9, 5.1 and 1.2 cm^3 mol^{-1} K, for **3-Tb**, **4-Dy**, **5-Er** and **6-Yb** respectively, due to thermal depopulation of the crystal field m_j states. For the presented compounds, magnetic coupling between the lanthanide ions has not been considered due to (i) the mononuclear nature of such compounds that lead to extensive Ln···Ln intermolecular distances and (ii) the well shielded nature of electrons in the 4f^n orbitals.[41]

The curves of the magnetization dependence with an external magnetic field, measured at a constant temperature of 2 K, are depicted in Fig. 7. None of the presented compounds shows saturation of the magnetization at 5 T ($g_j J$).[32]

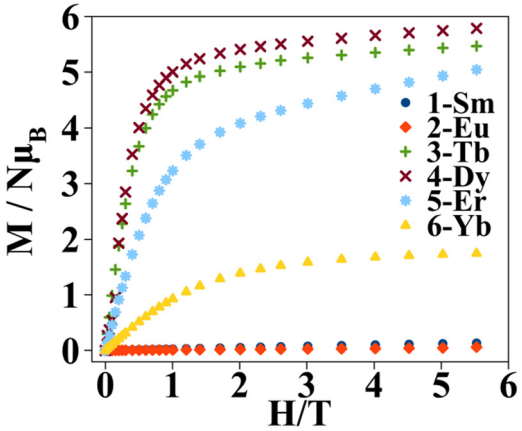

Fig. 7 Magnetization dependence with an external magnetic field measured at 2 K for compounds **1-Sm** to **6-Yb**.

Alternating current measurements. Moreover, alternating current (AC) magnetic susceptibility measurements were performed for all lanthanide samples except for **1-Eu**. Under a direct current external magnetic field (H_{dc}) of 0 T, only **4-Dy** showed slow relaxation of the magnetization and therefore single ion magnet (SIM) behaviour. Magnetic susceptibility imaginary component (χ_M'') shows maxima in the 2–18 K temperature range Fig. 8a. When cooling the sample down to 2 K, the χ_M'' values increase again, though a second peak is not observed. This is probably due to the Quantum Tunnelling of the Magnetization (QTM) mechanism that is taking place at such low temperatures.[41] The AC magnetic data were measured under an oscillating magnetic field of 4×10^{-4} T in the 1–1488 Hz frequency range Fig. 8b. χ_M'' maxima from the low temperature curves remain constant until a certain temperature where they move to higher frequencies upon increasing the temperature. This suggests that at low temperature the relaxation of the magnetization occurs *via* a temperature independent mechanism such as QTM whereas at the higher temperature range, thermally activated mechanisms, such as Orbach and/or Raman, are taking place.[42] In-phase and out-of-phase magnetic susceptibility representation (χ_M' *vs.* χ_M'') in the so called Cole–Cole plot show semicircles that are not perfectly symmetric, Fig. 8c.

The Cole–Cole plot can be fitted using the one component Generalized Debye model in the 2.5–13.5 K temperature range, eqn (S3) (ESI†)[43] The fits of the Cole–Cole curves of the different magnetic data were obtained using the CCFit software[44] (Table S4, ESI†). The α parameter quantifies the width distribution of the relaxation times of magnetization. For **4-Dy** α varies from 0.24 at 2.5 K to 0.03 at 13.5 K.

The semi-log representation of the relaxation of the magnetization times as function of temperature ($\ln(\tau)$ *vs.* $1/T$) is depicted in Fig. 9a. In the high temperature range a clear linear trend is observed. The linear segment is fitted following an Arrhenius type law, eqn (1). This model describes the thermally assisted Orbach relaxation of the magnetization mechanism taking place between the degenerate $\pm m_j$ ground state levels *via*

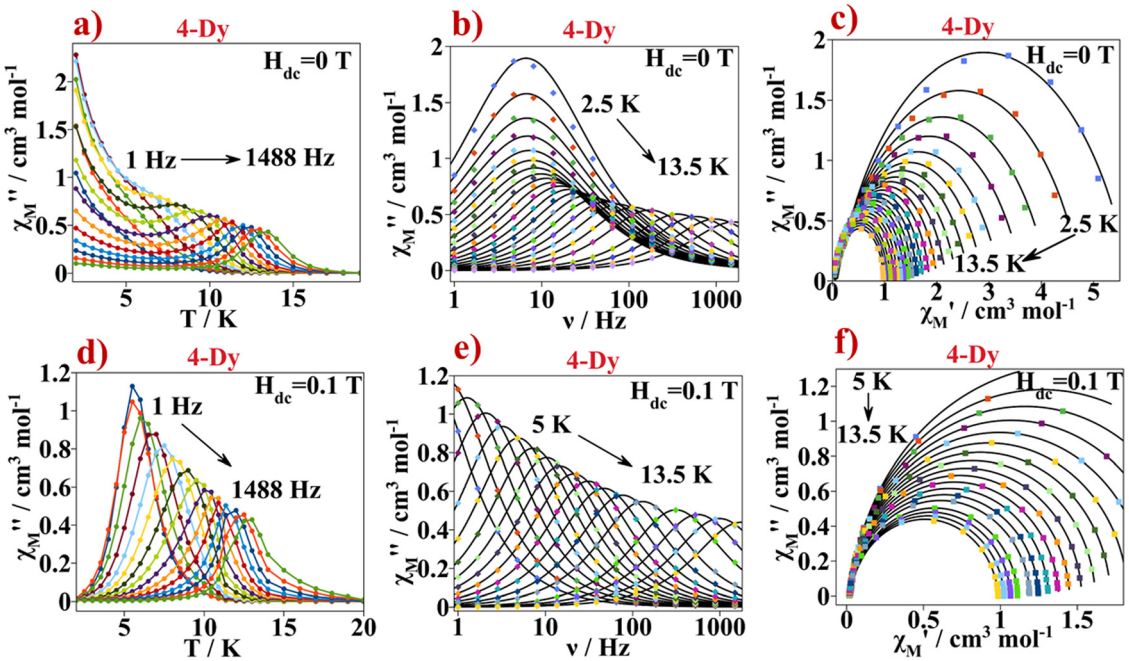

Fig. 8 (a) χ_M'' *versus* temperature plot obtained at a H_{dc} = 0 T for **4-Dy**. Continuous lines serve as an eye guide, (b) χ_M'' *versus* frequency plot obtained at a H_{dc} = 0 T for **4-Dy**. Continuous black lines correspond to the best fit according to eqn (S3) (ESI†), (c) Cole–Cole plot for **4-Dy** from the AC data recorded at a H_{dc} = 0 T. Continuous black line corresponds to the best fit according to eqn (S3) (ESI†), (d) χ_M'' *versus* temperature plot obtained at a H_{dc} = 0.1 T for **4-Dy**. Continuous lines serve as an eye guide, (e) χ_M'' *versus* frequency plot obtained at a H_{dc} = 0.1 T for **4-Dy**. Continuous black line corresponds to the best fit according to eqn (S3) (ESI†) and (f) Cole–Cole plot for **4-Dy** from the AC data measured at a H_{dc} = 0.1 T. Continuous black line corresponds to the best fit according to eqn S3 (ESI†).

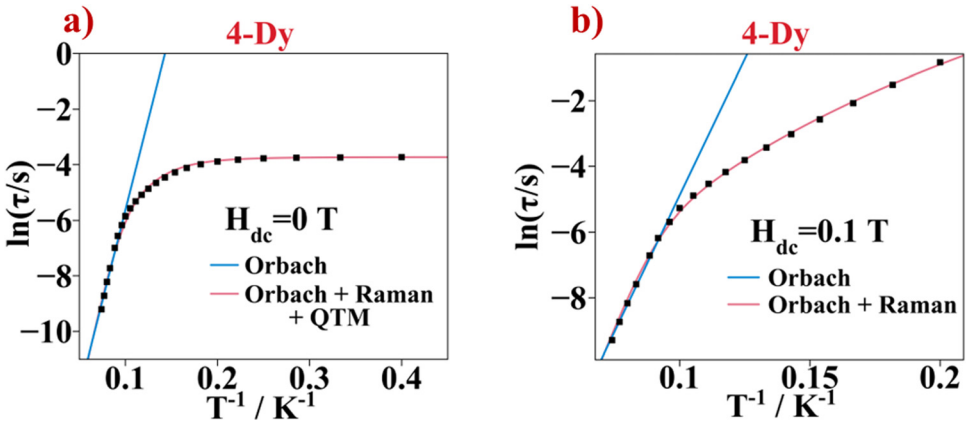

Fig. 9 (a) ln(τ) *vs.* 1/T plot of **5-Dy** obtained in the H_{dc} = 0 T. (b) ln(τ) *vs.* 1/T plot of **5-Dy** obtained in the H_{dc} = 0.1 T. In both figures, continuous lines represent the best fit using the stated equations of the relaxation of magnetization mechanisms.

an energetically higher excited m_j state of the Dy^{3+} ion.

$$\tau^{-1} = \tau_0^{-1}\exp\left(\frac{-\Delta E}{k_B T}\right) \quad (1)$$

By fitting the magnetic data in the 10–13.5 K temperature range using eqn (1), the effective energy barrier (ΔE) yielded 91.1 cm^{-1} and the pre-exponential factor (τ_0) was 7.2 × 10^{-9} s. However, the linear fashion is not followed along all the temperatures. This indicates the presence of another mechanism responsible for the relaxation of the magnetization under 13.5 K. On cooling the sample, the ln(τ) *vs.* T^{-1} curve enters a plateau region indicating that the spin of the lanthanide ion returns to the equilibrium phase *via* the faster QTM process. Consequently, the ln(τ) *vs.* T^{-1} curve was fitted with eqn (2) considering the three relaxation mechanisms. The best fit was obtained with ΔE = 103.7 cm^{-1} and τ_0 = 2.53 × 10^{-9} s for Orbach, C = 8.18 × 10^{-4} s^{-1} K^{-n} and n = 5.5 for Raman and τ_{QTM} = 0.03 s for the QTM processes.

$$\tau^{-1} = CT^n + \tau_0^{-1}\exp\left(\frac{-\Delta E}{k_B T}\right) + \tau_{QMT}^{-1} \quad (2)$$

To remove the QTM in the relaxation of the magnetization process of **4-Dy**, an external magnetic field can be applied while measuring the AC magnetic susceptibility response. An external magnetic field breaks the degeneracy between the $\pm m_j$ states so the fast QTM between the m_j levels is reduced or even eliminated.[41]

To establish the optimal H_{dc} for the Dy^{3+} sample, χ_M' and χ_M'' components were measured at constant temperature (11 K) and by applying different external magnetic fields, from 0 to 1.8 T. A plot of τ ($1/2\pi\omega$) *vs.* H_{dc} shows that the relaxation time is the greatest when the applied external magnetic field is 0.1 T. This DC field was found to be optimal, Fig. S17 (ESI†).

Fig. 8d and e show the AC measurement of **4-Dy** at H_{dc} of 0.1 T. Now, on cooling the sample, no increase of the χ_M'' component with temperature is observed, suggesting that the fastest relaxation mechanism observed at low temperatures in the H_{dc} = 0 experiments, QTM, is not present. The magnetic data were analysed in the temperature range where the χ_M'' *vs.* T peaks appear between 5 and 13.5 K. The χ_M'' *versus* the oscillating frequency relationship shows maxima that move progressively from lower frequency to higher frequency values as temperature increases, indicating a temperature dependent relaxation mechanism. The curves from the Cole–Cole plots, Fig. 8f, were fitted using the one component Generalized Debye model, and the obtained α values are in the range 0.02–0.05, Table S5 (ESI†).

The ln(τ) *versus* T^{-1} plot for H_{dc} = 0.1 T measurement is shown in Fig. 9b. A linear trend appears in the high temperature range corresponding to the Orbach relaxation mechanism. The linear part was fitted using the Arrhenius law giving ΔE = 109.3 cm^{-1} and τ_0 = 9.3 × 10^{-10} s. The trend of the ln(τ) *vs.* T^{-1} curve changes as the temperature decreases. Moreover, the plateau at low temperature seen in the ln(τ) *vs.* T^{-1} curve of the H_{dc} = 0 T measurement, corresponding to the QTM, is not seen anymore. Thus, the fitting was done taking out the QTM part of eqn (2). The best fit gave ΔE = 140.5 cm^{-1} and τ_0 = 3.6 × 10^{-11} s values for the Orbach mechanism and C = 1.10 × 10^{-4} s^{-1} K^{-n} and n = 6.2 values for the Raman mechanism.

The magnetic behaviour of the former compound is similar to other β-diketonate compounds with the DyO_6N_2 coordination environment. The ΔE value presented herein is similar to that obtained in other systems with the $Btfa^-$ β-diketonate ligand found in the literature.[45] The mononuclear compound with formula [Dy(Btfa)(bipy)][45a] shows SIM behaviour, but just a few maxima are found in the high frequency range. When applying an external magnetic field of 0.12 T, the QTM is reduced, and the SIM performance is improved with a ΔE of 62.9 cm^{-1}. Changing the polypyridyl ligand from bipy to 4,4′-dinonyl-2,2′-bipy (**6-Dy**) in the presented work, the SIM performance improves with a ΔE of 91.1 cm^{-1} at a 0 DC external magnetic field and it is enhanced to 109 cm^{-1} when a H_{dc} of 0.1 T is applied.

The magnetic anisotropy axis of the m_j = ±15/2 state can be calculated using a simple electrostatic model presented by the Chilton Group.[46] To enhance the SMM behavior, the $\pm m_j$ ground state stabilized by the crystal field should be the one

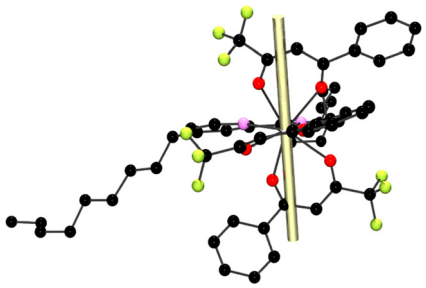

Fig. 10 Orientation of the magnetic anisotropy axis of the m_j = ±15/2 state (yellow rod) of compound **4-Dy**.

with the greatest value: ±15/2, for a Dy^{3+} ion, which has an oblate electron density. Therefore, to stabilize this m_j state, an axially stressed coordination environment should be induced. The more electron-rich atoms (O atoms from the β-diketonate ligands in this case) should be in the axial positions. Generally, the atoms with highly electron-rich atoms will form the shortest Dy-donor atom bond distances. Therefore, by calculating the anisotropy axis, if it passes through the shortest Dy–O bond distances of the more electronegative atoms, this will indicate that the m_j ground state is in its major contribution of ±15/2 (the largest m_j value). To calculate the anisotropic axis from the crystallographic data, the Magellan program, which can only be used for Dy^{3+} ions, was used. Fig. 10 shows the magnetic axis in yellow, and it goes along the Dy–O bonds formed by Dy–O2 and Dy–O5 with the shortest bond distances which are 2.311 and 2.320 Å, respectively. We can conclude that the stabilized m_j ground state of compound **4-Dy** is ±15/2.

The remaining lanthanide compounds, **3-Tb**, **5-Er** and **6-Yb**, showed slow relaxation of the magnetization just when an external magnetic field was applied. The magnetic response of such complexes was measured under the optimal H_{dc} = 0.1 T for **3-Tb** and **6-Yb** and 0.05 T for **5-Er**, Fig. S16 and S17 (ESI†). The plots of the out-of-phase magnetic susceptibility components varying with temperature and frequency are depicted in Fig. 11 for **3-Tb**, **5-Er** and **7-Yb**.

For **3-Tb**, the maximum values of χ_M'' appear upon cooling the sample down to the liquid helium temperature and at high oscillating frequencies. Nevertheless, the Cole–Cole plots for **3-Tb** are uncompleted asymmetric semicircles that can be fitted

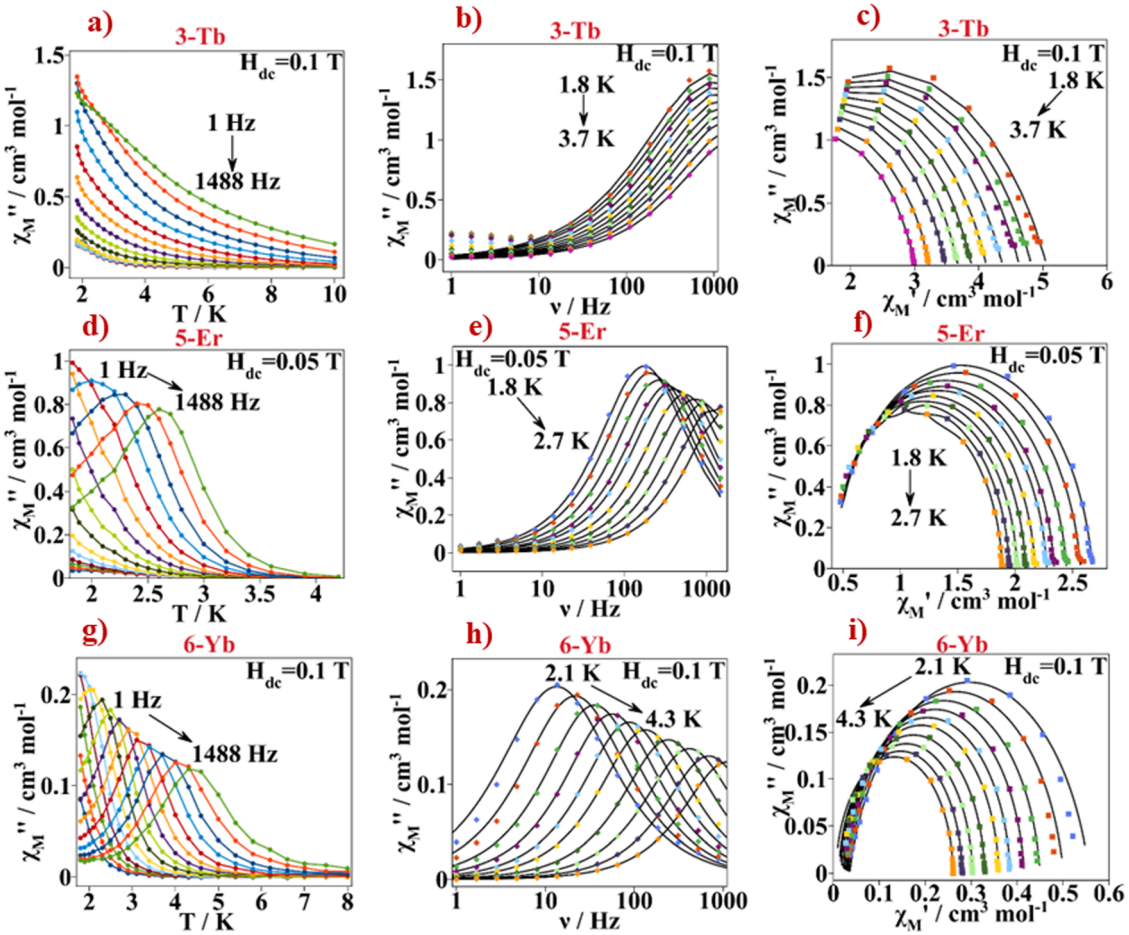

Fig. 11 (a), (d) and (g) temperature dependence of χ_M'' for **3-Tb**, **5-Er** and **6-Yb** respectively. Continuous lines serve as an eye guide. (b), (e) and (h) χ_M'' *versus* frequency characteristics for **3-Tb**, **5-Er** and **6-Yb** respectively. Continuous black lines correspond to the best fit according to eqn (S3) (ESI†). (c), (f), (i) Cole–Cole plots for compounds **3-Tb**, **5-Er** and **6-Yb** respectively. Continuous black lines correspond to the best fit according to eqn (S3) (ESI†). The AC data were recorded with H_{dc} = 0.1 T for **3-Tb** and **6-Yb** and 0.05 T for **5-Er**.

using the one component Debye model with α values of 0.3 to 0.23 on increasing temperature, Table S6 (ESI†). The $\ln(\tau)$ *vs.* T^{-1} plot is shown in Fig. 12a. No linear trend is followed along the temperature axes, indicating that the relaxation of the magnetization of the Tb^{3+} compound does not occur through the Orbach process. Clearly, a temperature dependence of the relaxation times is observed, therefore the Raman process can be considered. The best fit of the magnetic data of **3-Tb** is obtained when both, Raman and Direct mechanism, are considered with values of C = 0.93 s^{-1} K^{-n} and n = 5.21 for the Raman and of A = 3275.1 s^{-1} K^{-1} for the Direct process. The terbium(III) ion has a $^7F_6$ ground state. When the Tb^{3+} ion is coordinated to ligand molecules forming a coordination compound, J splits into $2J + 1$ $\pm m_j$ states due to the crystal field effect. For J equal to 6, that would be 13 m_j sublevels comprised between +6 to −6. Due to the non-Kramer nature of the Tb^{3+} ion, a certain crystal field can stabilize the m_j ground state with the lower value which in this case would be m_j = 0. If this occurred, then no relaxation of the magnetization nor SMM behaviour could be seen at all. For a Tb^{3+} compound showing SMM behaviour, the crystal field should optimize the oblate shaped electron density m_j state with larger value (m_j = 6). Therefore, the crystal field of compound **3-Tb** stabilizes a ground state different than m_j = 0, though there is transverse contribution in the ground state wavefunction because of QTM presence at H_{dc} = 0 T and even applying an optimal external magnetic field, slow relaxation of the magnetization is recorded but in a very narrow temperature range.[47]

Compounds **5-Er** and **6-Yb** show clear maxima of the χ_M'' component in a rather low temperature range (1.8–2.7 K for **5-Er** and of 2.1–4.3 K for **6-Yb**). For **5-Er** and **6-Yb**, in the plots of the out-of-phase magnetic susceptibility components *versus* temperature and frequency, the χ_M'' peaks move progressively to higher frequencies upon increasing the temperature. The Cole–Cole plots show non-symmetric semicircles, Fig. 11c, f and i. For **5-Er** and **6-Yb**, Cole–Cole curves could be fitted with the one component Generalized Debye model equation, eqn (S3) and Tables S7 and S8 (ESI†). The α values obtained from the fit are in the range of 0.08 to 0.03 (for **5-Er**) and of 0.16 to 0.02 (for **6-Yb**) on increasing temperature. Relaxation of magnetization times with temperature characteristics are plotted in Fig. 12b and c.

For the **5-Er** compound, the Arrhenius law is used to fit the linear segment in the higher temperature range. The obtained effective energy barrier is 13.0 cm^{-1} and the pre-exponential factor is 8.75 × 10^{-8} s. The linear trend is not followed along the curve, therefore a function with the equation including the Orbach and Raman relaxation mechanisms (first two components in eqn (2)) gives the best fit. The obtained parameters are ΔE = 24.6 cm^{-1}, τ_0 = 8.75 × 10^{-8} s, C = 96.1 s^{-1} K^{-n} and n = 4.05. Finally, for compound **6-Yb**, the magnetic data cannot be fitted using the Arrhenius law since there is no clear linear trend in the higher temperature range and therefore the relaxation of the magnetization by the Orbach process is excluded. The best fit of the $\ln(\tau)$ *vs.* T^{-1} curves is acquired when equations describing the Raman and Direct relaxation of the magnetization processes are considered, eqn (3), and the obtained parameters are C = 0.51 s^{-1} K^{-n}, n = 6.5 and A = 8.58 s^{-1} K^{-1}. Other Yb^{3+} coordination compounds where the slow relaxation of the magnetization process is dominated by Raman and Direct mechanisms rather than Orbach, are found in the literature.[48] A compilation of the fitted parameters for all compounds is found in Table S9 (ESI†).

$$\tau^{-1} = CT^n + AT \quad (3)$$

It is important to consider that the low temperature range in which the **3-Tb**, **5-Er** and **6-Yb** compounds show slow relaxation of the magnetization is very narrow and therefore not many values of τ can be extracted. Added to the over-parametrization when using the different combinations of the equations (Raman, Direct, Orbach, QTM, Local mode) to acknowledge the relaxation of the magnetization mechanisms, it becomes difficult to extract accurate conclusions.

4.4. Correlation between magnetic and spectroscopic data

The relaxation of magnetization energy barrier described by the Orbach mechanism of **4-Dy** calculated by means of the magnetic data can be compared with the energy barrier calculated through the spectroscopic data. The emission spectrum of **4-Dy**

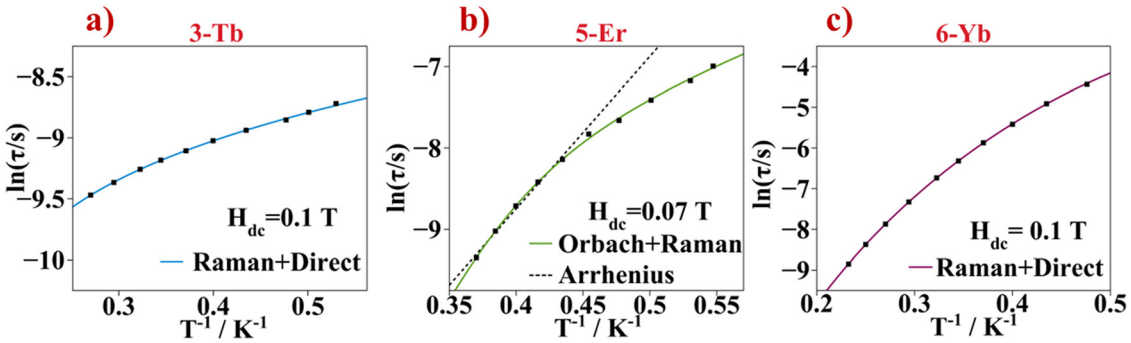

Fig. 12 (a) $\ln(\tau)$ *vs.* $1/T$ plot of (a) **3-Tb**, (b) **5-Er** and (c) **6-Yb** obtained at the H_{dc} = 0.1, 0.07 and 0.1 T respectively. In the three figures, continuous lines represent the best fit using the stated equations of the relaxation of magnetization mechanisms. The black dotted line in (b) represents the fit in the high temperature range following an Arrhenius law.

was obtained at T = 77 K configuring the experiment to use a slower acquisition time. By measuring the emission spectrum at such low temperature, the corresponding $\pm m_j$ energy levels formed by the crystal field splitting can be distinguished. Assuming that only the first m_j state of the $^4F_{9/2}$ emitting level is populated and that at such low temperature we can reduce, as much as possible, the presence of hot bands and vibronic side bands, the $^6H_{15/2}$ ground state of the Dy^{3+} Kramer ion splits due to the crystal field effect by $J + 1/2$ states: $\pm m_j = \pm 15/2$, $\pm 13/2$, $\pm 11/2$, $\pm 9/2$, $\pm 7/2$, $\pm 5/2$, $\pm 3/2$, $\pm 1/2$.

A multi-Gaussian function fit is performed for the $^7F_{9/2} \rightarrow {}^6H_{15/2}$ emission band, Fig. S18 (ESI†). Different trials with more than eight Gaussian functions were performed to include the 'hot bands'. A good fit is obtained when 9 Gaussian functions are used. The ninth Gaussian function covers the small shoulder at the low energy range. This indicates that even at low temperatures the side emission bands such as the 'hot bands' are still present. They can appear even at lower temperatures as demonstrated in other published studies.[49] Thus, the first two bands that are higher in energy are assigned to the zero phonon $0' \rightarrow 0$ and $0' \rightarrow 1$ transitions. The energy difference between the peaks of the two first Gaussian functions is 93.8 cm^{-1}. Attending to the calculated ΔE value from the magnetic data (91 cm^{-1}), the Orbach relaxation process occurs only through the first $\pm m_j$ excited state. This could consider the fact that the thermally activated relaxation of the magnetization process (Orbach) does not take place through the whole energy barrier composed by all the $\pm m_j$ states of the Dy^{3+} ion but only *via* the first $\pm m_j$ excited state.

Moreover, the emission spectra of the **6-Yb** compounds measured, also, at 77 K show that the $^2F_{5/2} \rightarrow {}^2F_{7/2}$ emission transition is split due to crystal field into four well distinguished peaks. The Yb^{3+} $^2F_{7/2}$ ground state break of the degeneracy due to crystal field splitting, should lead to four $\pm m_j$ states ($\pm 7/2$, $\pm 5/2$, $\pm 3/2$, $\pm 1/2$). A multi-Gaussian fit of the emission spectra is performed successfully with four Gaussian functions, Fig. S19 (ESI†). The splitting between the peaks is as follows: 25.1 (1st–2nd), 13.6 (2nd–3rd) and 17.7 cm^{-1} (3rd–4th). The dynamic magnetic data for **6-Yb** show that the magnetization does not relax through an effective energy barrier *via* the Orbach process.

5. Conclusions

Six new β-diketonate lanthanide coordination compounds have been synthesized and fully characterized spectroscopically and magnetically. The new mononuclear compounds with formula $[Ln(btfa)_3(4,4'\text{-dinonylbipy})]$ Ln = Sm (**1-Sm**), Eu (**2-Eu**), Tb (**3-Tb**), Dy (**4-Dy**), Er (**5-Er**) and Yb (**6-Yb**) have been isolated through the reaction of $[Ln(btfa)_3(H_2O)_2]$ ($btfa^-$ = 4,4,4-trifluoro-1-phenyl-1,3-butanedionate) with 4,4′-dinonyl-2,2′-bipyridyl (4,4′-dinonylbipy) in ethanol. The structural characterization has been carried out by single crystal X-ray diffraction and by X-ray powder diffraction.

Photoluminescence studies were performed for all complexes in $CHCl_3$ solution and in solid state. Furthermore the solid samples were also measured at the liquid nitrogen temperature (77 K). All polycrystalline samples show sensitized luminescence when exciting the samples at the ligand excitation band indicating an effective antenna effect.

Luminescence quantum yield could be measured for the visible light emitters **1-Sm**, **2-Eu**, **3-Tb**, and **4-Dy** in chloroform solution and in solid state, with the europium compound yielding the highest value of 0.68 in polycrystalline sample and of 0.42 in solution. Moreover, luminescence decay lifetime was measured for the **1-Sm** and **2-Eu** compounds with the **2-Eu** polycrystalline sample showing the greatest τ_{obs} = 0.90 ms.

Owing to the peripheral alkyl and $-CF_3$ groups of the 4,4′-dinonyl-2,2′-bipy and $btfa^-$ ligands, the **2-Eu** and **6-Yb** complexes showed a relatively low sublimation temperature, around 140–150 °C at $\sim 10^{-6}$ mbar, hence they are promising materials for OLEDs. Considering the good luminescence properties of the **2-Eu** complex and intriguing long wavelength PL of **6-Yb** they were selected to produce vacuum deposited OLEDs. The **2-Eu** based OLED showed an external quantum efficiency of 2.0–2.1% and luminance in a range $\sim$200–600 cd m^{-2}. Using **6-Yb** as the emitter gave a near infrared electroluminescence at $\sim$1000 nm with an EQE of 0.1–0.17%.

From the magnetic study of this series of compounds, dynamic magnetic measurements proved that **5-Dy** display SIM behaviour at relatively high temperatures showing maximum values of the χ_M'' component up to 14 K. The phonon lattice mechanism dominating in the high temperature range is the Orbach process with an effective energy barrier of 91.1 cm^{-1}. Moreover, at intermediate temperatures the Raman mechanism is present and the process of quantum nature, QTM, governs the relaxation of the magnetization at the low temperature range. By applying an optimal DC magnetic field of 0.1 T the QTM is removed, and the magnetic relaxation is still dominated by the Orbach process at high temperatures with a greater ΔE value of 109.3 cm^{-1} than that found at H_{dc} = 0 T. The Raman mechanism is involved while cooling the sample. Magnetic and spectroscopic studies of **5-Dy** showed that the thermal activated relaxation of the magnetization process (Orbach) does not take place through the whole energy barrier composed of all the $\pm m_j$ states of the Dy^{3+} ion but only *via* the first $\pm m_j$ excited state. In addition, **3-Tb**, **5-Er** and **6-Yb** show slow relaxation of the magnetization under an external applied magnetic field. The mechanisms that best describe the relaxation of the magnetization of these three compounds resulted in a combination of Raman and Direct for **3-Tb** and **6-Yb** and Orbach and Raman for the **5-Er** analogue.

Conflicts of interest

There are no conflicts to declare.

Acknowledgements

R. V. and A. T. acknowledge the financial support from Ministerio de Ciencia, Innovación y Universidades (Spain), Project PGC2018-094031-B-100.

References

1 N. Ishikawa, M. Sugita, T. Ishikawa, S. Y. Koshihara and Y. Kaizu, Lanthanide Double-Decker Complexes Functioning as Magnets at the Single-Molecular Level, *J. Am. Chem. Soc.*, 2003, **125**, 8694–8695.

2 (*a*) J. Tang and P. Zhang, *Lanthanide Single Molecule Magnets*, Springer-Verlag, Berlin Heidelberg, 2015; (*b*) H. L. C. Feltham and S. Brooker, Review of purely 4f and mixed-metal nd-4f single-molecule magnets containing only one lanthanide ion, *Coord. Chem. Rev.*, 2014, **276**, 1–33; (*c*) D. N. Woodruff, R. E. P. Winpenny and R. A. Layfield, Lanthanide Single-Molecule Magnets, *Chem. Rev.*, 2013, **113**, 5110–5148; (*d*) A. Borah and R. Murugavel, Magnetic relaxation in single-ion magnets formed by less-studied lanthanide ions Ce(III), Nd(III), Gd(III), Ho(III), Tm(II/III) and Yb(III), *Coord. Chem. Rev.*, 2022, **453**, 214288; (*e*) D. N. Woodruff, F. Tuna, M. Bodensteiner, R. E. P. Winpenny and R. A. Layfield, Single-Molecule Magnetism in Tetrametallic Terbium and Dysprosium Thiolate Cages, *Organometallics*, 2013, **32**, 1224–1229; (*f*) S. Zhang, H. Ke, Q. Shi, J. Zhang, Q. Yang, Q. Wei, G. Xie, W. Wang, D. Yang and S. Chen, Dysprosium(III) complexes with a square-antiprism configuration featuring mononuclear single molecule magnetic behaviours based on diferent β-diketonate ligands and auxiliary ligands, *Dalton Trans.*, 2016, **45**, 5310–5320; (*g*) L. Razquin-Bobillo, O. Pajuelo-Corral, A. Zabala-Lekuona, A. Rodríguez-Diéguez and J. Cepeda, An experimental and theoretical study of the.magnetic relaxation in heterometallic coordination polymers based on 6-methyl-2-oxonicotinate and lanthanide(III) ions with square antriprismatic environament, *Dalton Trans.*, 2022, **51**, 16243–16255.

3 (*a*) F.-S. Guo, B. M. Day, Y.-C. Chen, M.-L. Tong, A. Mansikkamäki and R. A. Layfield, A Dysprosium Metallocene Single-Molecule Magnet Functioning at the Axial Limit, *Angew. Chem., Int. Ed.*, 2017, **56**, 11445–11449; (*b*) C. A. P. Goodwin, F. Ortu, D. Reta, N. F. Chilton and D. P. Mills, Molecular magnetic hysteresis at 60 kelvin in dysprosocenium, *Nature*, 2017, **548**, 439–442.

4 F.-S. Guo, B. Day, Y.-C. Chen, M. L. Tong, A. Mansikkamäki and R. A. Layfield, Magnetic hysteresis up to 80 kelvin in a dysprosium metallocene single-molecule magnet, *Science*, 2018, **362**, 1400–1403.

5 Y. Hasegawa, Y. Kitagawa and T. Nakanish, Effective photosensitized, electrosensitized, and mechanosensitized luminescence of lanthanide complexes, *NPG Asia Mater.*, 2018, **10**, 52–70.

6 (*a*) J.-C. G. Bünzli, On the design of highly luminescent lanthanide complexes, *Coord. Chem. Rev.*, 2015, **293–294**, 19–47; (*b*) G. F. de Sá, O. L. Malta, C. de Mello Donegá, A. M. Simas, R. L. Longo and P. A. Santa-Cruz, Spectroscopic Properties and Design of Highly Luminescent Lanthanide Coordination Complexes, *Coord. Chem. Rev.*, 2000, **196**, 165–195.

7 G. Huang, G. Calvez, Y. Suffren, C. Daiguebonne, S. Freslon, O. Guillou and K. Bernot, Closing the Circle of the Lanthanide-Murexide Series: Single-Molecule Magnet Behavior and Near-Infrared Emission of the Nd^{III} Derivative, *Magnetochemistry*, 2018, **4**, 44, DOI: **10.3390/magnetochemistry4040044**.

8 B. Casanovas, M. Font-Bardía, S. Speed, M. S. El Fallah and R. Vicente, Field Induced SMM and Visible/NIR-luminescence behaviour for dinuclear Ln(III) complexes with 2-fluorobenzoate, *Eur. J. Inorg. Chem.*, 2018, 1928–1937.

9 (*a*) H.-Y. Chen, W.-M. Wang, H.-L. Gao and J.-Z. Cui, *RSC Adv.*, 2016, **6**, 34165–34174; (*b*) S. Bala, M. S. Bishwas, B. Pramanik, S. Khanra, K. M. Fromm, P. Poddar and R. Mondal, Construction of Polynuclear Lanthanide (Ln = DyIII, TbIII, and NdIII) Cage Complexes Using Pyridine−Pyrazole-Based Ligands: Versatile Molecular Topologies and SMM Behavior, *Inorg. Chem.*, 2015, **54**, 8197–8206.

10 L. A. Galán, S. Wada, L. Cameron, A. N. Sobolev, Y. Hasegawa, E. Zysman-Colman, M. I. Ogden and M. Massi, Photophysical investigation of near infrared emitting lanthanoid complexes incorporating tris(2-naphthoyl) methane as a new antenna ligand, *Dalton Trans.*, 2019, **48**, 3768–3776.

11 C. Yang, L. M. Fu, Y. Wang, J. P. Zhang, W. T. Wong, X.-C. Ai, F. Y. Qiao, B. S. Zou and L.-L. Gui, A Highly Luminescent Europium Complex Showing Visible-Light-Sensitized Red Emission: Direct Observation of the Singlet Pathway, *Angew. Chem., Int. Ed.*, 2004, **116**, 5120–5123.

12 (*a*) D. Imbert, M. Cantuel, J.-C. G. Bunzli, G. Bernardinelli and C. Piguet, Extending Lifetimes of Lanthanide-Based Near-Infrared Emitters (Nd, Yb) in the Millisecond Range through Cr(III) Sensitization in Discrete Bimetallic Edifices, *J. Am. Chem. Soc.*, 2003, **125**, 15698–15699; (*b*) A. Beeby, B. P. Burton-Pye, S. Faulkner, G. R. Motson, J. C. Jeffery, J. A. McCleverty and M. D. Ward, Synthesis and near-IR luminescence properties of neodymium(III) and ytterbium(III) complexes with poly(pyrazolyl)borate ligands, *J. Chem. Soc., Dalton Trans.*, 2002, 1923–1928.

13 (*a*) W. Li, J. Li, H. Li, P. Yan, G. Hou and G. Li, NIR luminescence of 2-(2,2,2-trifluoroethyl)-1-indone (TFI) neodymium and ytterbium complexes, *J. Lumin.*, 2014, **146**, 205–210; (*b*) X. Wang, L. Wang, Y. Luo, W. Wu, X. Tian, Q. Zhang and B. Chen, NIR luminescence of a visible-light-sensitized neodymium complex with large experimental fluorescence branching ratio for 4F3/2 → 4I11/2 in PMMA, *J. Mater. Res.*, 2011, **26**, 1517–1523.

14 (*a*) S. D. Bennett, S. J. A. Pope and B. D. Ward, Near-IR luminescent neodymium complexes: spectroscopic probes for hydroamination catalysis, *Chem. Commun.*, 2013, **49**, 6072–6074; (*b*) N. M. Shavaleev, R. Scopelliti, F. Gumy and J.-C. G. Bünzli, Near-Infrared Luminescence of Nine-Coordinate Neodymium Complexes with Benzimidazole-Substituted 8-Hydroxyquinolines, *Inorg. Chem.*, 2008, **47**, 9055–9068.

15 (*a*) S. Comby and J.-C. G. Bünzli, Lanthanide Near-Infrared Luminescence in Molecular Probes and Devices, *Handbook on the Physics and Chemistry of Rare Earths*, Elsevier, Amsterdam, The Netherlands, 2007, vol. 37, pp. 217–470;

(*b*) Y. Hasegawa and T. Nakanishi, Luminescent lanthanide coordination polymers for photonic applications, *RSC Adv.*, 2015, **5**, 338–353; (*c*) Y. Hasegawa, Photofunctional Lanthanoid Complexes, Coordination Polymers, and Nanocrystals for Future Photonic Applications, *Bull. Chem. Soc. Jpn.*, 2014, **87**, 1029–1057.

16 (*a*) J.-L. Liu, Y.-C. Chen and M.-L. Tong, Symmetry strategies for high performance lanthanide-based single-molecule magnets, *Chem. Soc. Rev.*, 2018, **47**, 2431–2453; (*b*) S. V. Eliseeva and J.-C. G. Bünzli, Lanthanide luminescence for functional materials and bio-sciences, *Chem. Soc. Rev.*, 2010, **39**, 189–227.

17 J.-C. G. Bünzli, Luminescence Bioimaging with Lanthanide Complexes, in *Luminescence of Lanthanide Ions in Coordination Compounds and Nanomaterials*, ed. A. De Bettencourt-Dias, John Wiley & Sons, Chichester, 2014, ch. 4, pp. 125–196.

18 (*a*) Y. Ding, Y. Wang, H. Li, Z. Duan, H. Zhang and Y. Zheng, Photostable and efficient red-emitters based on zeolite L crystals, *J. Mater. Chem.*, 2011, **21**, 14755–14759; (*b*) R. Ilmi, S. Kanslz, N. Dege and M. S. Khan, Synthesis, structure, Hirshfeld surface analysis and photophysical studies of red emitting europium acetylacetonate complex incorporating a phenanthroline derivative, *J. Photochem. Photobiol., A*, 2019, **377**, 268–281; (*c*) P. P. F. da Rosa, Y. Kitagawa and Y. Hasegawa, Luminescent lanthanide complex with seven-coordination geometry, *Coord. Chem. Rev.*, 2020, **406**, 213153; (*d*) Z. Ahmed and K. Iftikhar, Red, orange-red and near-infrared light emitting ternary lanthanide tris β-diketonate complexes with distorted C_{4v} geometrical structures, *Dalton Trans.*, 2019, **48**, 4973–4986; (*e*) J. Li, H. Li, P. Yan, P. Chen, G. Hou and G. Li, Synthesis, Crystal Structure, and Luminescent Properties of 2-(2,2,2-Trifluoroethyl)-1-indone Lanthanide Complexes, *Inorg. Chem.*, 2012, **51**, 5050–5057; (*f*) R. Ilmi, M. S. Khan, Z. Li, L. Zhou, W.-Y. Wong, F. Marken and P. R. Raithby, Utilization of Ternary Europium Complex for Organic Electroluminescent Devices and as a Sensitizer to Improve Electroluminescence of Red-Emitting Iridium Complex, *Inorg. Chem.*, 2019, **58**, 8316–8331; (*g*) R. Ishimatsu, E. Kunisawa, K. Nakano, C. Adach and T. Imato, Electrogenerated Chemiluminescence and Electronic States of Several Organometallic Eu(III) and Tb(III) Complexes: Effects of the Ligands, *ChemistrySelect*, 2019, **4**, 2815–2831; (*h*) L. Arrué, J. Santoyo-Flores, N. Pizarro, X. Zarate, D. Páez-Hernández and E. Schott, The role played by structural and energy parameters of β-Diketones derivatives as antenna ligands in Eu(III) complexes, *Chem. Phys. Lett.*, 2021, **773**, 138600.

19 J. Long, Y. Guari, R. A. S. Ferreira, L. D. Carlos and J. Larionova, Recent advances in luminescent lanthanide based Single-Molecule Magnets, *Coord. Chem. Rev.*, 2018, **363**, 57–70.

20 R. Vicente, À. Tubau, S. Speed, F. A. Mautner, F. Bierbaumer, R. C. Fischer and S. S. Massoud, Slow magnetic relaxation and luminescence properties in neodymium(III) 4,4,4-trifluoro-1-(2-naphthyl)butane-1,3-dionato complexes incorporating bipyridyl ligands, *New J. Chem.*, 2021, **45**, 14713–14723.

21 S. Speed, À. Tubau, R. Vicente, E. Castro and M. Font-Bardía, Slow Magnetic Relaxation and Luminescence Properties in Tetra β-diketonate Lanthanide(III) Complexes, *Magnetochemistry*, 2023, **9**, 131–145.

22 J. Kido, H. Hayase, K. Hongawa, K. Nagai and K. Okuyama, *Appl. Phys. Lett.*, 1994, **65**, 2124–2126.

23 (*a*) H. Xua, Q. Sun, Z. An, Y. Wei and X. Liu, Electroluminescence from europium(III) complexes, *Coord. Chem. Rev.*, 2015, **293–264**, 228–249; (*b*) R. Ilmi, X. Li, N. K. Al Rasbi, L. Zhou, W.-Y. Wong, P. R. Raithby and M. S. Khan, Two new red-emitting ternary europium(III) complexes with high photoluminescence quantum yields and excepcional performance in OLED devices, *Dalton Trans.*, 2023, **52**, 12885–12891.

24 Bruker APEX, *SAINT v. 8.37A*, Bruker AXS Inc., Madison, WI, USA, 2015.

25 G. M. Sheldrick, *SADABS v. 2*, University of Goettingen, Goettingen, Germany, 2001.

26 G. M. Sheldrick, Crystal structure refinement with SHELXL, *Acta Crystallogr., Sect. C: Struct. Chem.*, 2015, **71**, 3–8.

27 C. F. Macrae, P. R. Edington, P. McCabe, E. Pidcock, G. P. Shields, R. Taylor, T. Towler and J. J. van de Streek, Mercury: Visualization and analysis of crystal structures. *Appl. Cryst*. 2006, **39**, 453–457.

28 A. L. Spek, *PLATON, a Multipurpose Crystallographic Tool; Utrecht University: Utrecht*, The Netherlands, 1999.

29 D. de Sa Pereira, A. P. Monkman and P. Data, Production and Characterization of Vacuum Deposited Organic Light Emitting Diodes, *J. Vis. Exp.*, 2018, **141**, e56593, DOI: **10.3791/56593**.

30 M. Llunell, D. Casanova, J. Cirera, P. Alemany and S. Alvarez, Shape Program. version 2, Universitat de Barcelona, Barcelona, Spain, 2010.

31 P. Alemany, D. Casanova, S. Alvarez, C. Dryzun and D. Avnir, Continuous Symmetry Measures: A New Tool in Quantum Chemistry, *Rev. Comput. Chem.*, 2017, **30**, 289–352, DOI: **10.1002/9781119356059.ch7**.

32 (*a*) *The Rare Earth Elements: Fundamentals and Applications*, ed. D. A. Atwood, John Wiley & Sons Ltd, 2012; (*b*) *Luminescence of Lanthanide Ions in Coordination Compounds and Nanomaterials*, ed. A. de Bettencourt-Dias, John Wiley & Sons Ltd, 2014.

33 C. M. Reddy, B. D. P. Raju, N. J. Sushma, N. S. Dhoble and S. J. Dhoble, *Renewable Sustainable Energy Rev.*, 2015, **5**, 566–584.

34 K. Binnemans, Interpretation of europium(III) spectra, *Coord. Chem. Rev.*, 2015, **295**, 1.

35 (*a*) W. T. Carnall, P. R. Fields and K. Rajnak, Electronic Energy Levels in the Trivalent Lanthanide Aquo Ions. I. Pr^{3+}, Nd^{3+}, Pm^{3+}, Sm^{3+}, Dy^{3+}, Ho^{3+}, Er^{3+}, and Tm^{3+}, *J. Chem. Phys.*, 1968, **49**, 4424–4442; (*b*) X. Yu, J. Peng, Z. Shi, Y. Shen, Z. Zhang and G. Li, Tubular solids of lanthanide-doped polyoxometalates in micrometer-scale: synthesis and NIR-

luminescent properties, *J. Lumin.*, 2015, **160**, 289–292; (*c*) À. Tubau, F. Zinna, L. Di Bari, M. Font-Bardía and R. Vicente, Luminescence, CPL and magnetic properties of 1D enantiopure Ln^{3+} complexes with (S-) and (R-) α-methoxyphenylacetate ligand, *Dalton Trans.*, 2023, **52**, 1122–1132; (*d*) J. Feng, L. Zhou, S.-Y. Song, A.-F. Li, W.-F. Li, W.-Q. Fan, L.-N. Sun, Y.-N. Yu and H.-J. Zhang, A study on the near-infrared luminescent properties of xerogel materials doped with dysprosium complexes, *Dalton Trans.*, 2009, 6593–6598; (*e*) M. Pan, B.-B. Du, Y.-X. Zhu, M.-Q. Yue, Z.-W. Wei and C.-Y. Su, Highly Efficient Visible-to-NIR Luminescence of Lanthanide(III) Complexes with Zwitterionic Ligands Bearing, *Chem. – Eur. J.*, 2016, **22**, 2440–2451; (*f*) S. Biju, N. Gopakumar, J.-C. G. Bünzli, R. Scopelliti, H. K. Kim and M. L. P. Reddy, Brilliant Photoluminescence and Triboluminescence from Ternary Complexes of DyIII and TbIII with 3-Phenyl-4-propanol-5-isoxazolonate and a Bidentate Phosphine Oxide Coligand, *Inorg. Chem.*, 2013, **52**, 8750–8758.

36 M. Latva, H. Takalo, V.-M. Mukkala, C. Matachescu, J. C. Rodríguez-Ubis and J. Kankare, Correlation between the lowest triplet state energy level of the ligand and lanthanide(III) luminescence quantum yield, *J. Lumin.*, 1997, **75**, 149–169.

37 (*a*) A. Aebischer, F. Gumy and J.-C. G. Bünzli, Intrinsic quantum yields and radiative lifetimes of lanthanide tris(dipicolinates), *Phys. Chem. Chem. Phys.*, 2009, **11**, 1346–1353; (*b*) S. Sato and M. Wada, Relations between Intramolecular Energy Transfer Efficiencies and Triplet State Energies in Rare Earth β-diketone Chelates, *Bull. Chem. Soc. Jpn.*, 1970, **43**, 1955–1962; (*c*) C. R. De Silva, J. Li, Z. Zheng and L. R. Corrales, Correlation of calculated excited-state energies and experimental quantum yields of luminescent Tb(III) β-diketonates, *J. Phys. Chem. A*, 2008, **112**(20), 4527–4530.

38 (*a*) S. Biju, Y. K. Eom, J.-C. G. Bünzli and H. K. Kim, A new tetrakis β-diketone ligand for NIR emitting Ln III ions: Luminescent doped PMMA films and flexible resins for advanced photonic applications, *J. Mater. Chem. C*, 2013, **1**, 6935–6944; (*b*) J. Bolton, New NIR emission from Sm^{3+} in Yb^{3+}-Sm^{3+} co-doped tellurite glass, *J. Lumin.*, 2021, **231**, 117717; (*c*) H. F. Brito, O. L. Malta, M. C. F. C. Felinto, E. E. S. Teotonio, J. F. S. Menezes, C. F. B. Silva, C. S. Tomiyama and C. A. A. Carvalho, Luminescence investigation of the Sm(III)-β-diketonates with sulfoxides, phosphine oxides and amides ligands, *J. Alloys Compd.*, 2002, **344**, 293–297; (*d*) L.-N. Sun, J.-B. Yu, H.-J. Zhang, Q.-G. Meng, E. Ma, C.-Y. Peng and K.-Y. Yang, Near-infrared luminescent mesoporous materials covalently bonded with ternary lanthanide [Er(III), Nd(III), Yb(III), Sm(III), Pr(III)] complexes, *Microporous Mesoporous Mater.*, 2007, **98**, 156–165.

39 M. H. V. Werts, R. T. F. Jukes and J. W. Verhoeven, The emission spectrum and the radiative lifetime of Eu^{3+} in luminescent lanthanide complexes, *Phys. Chem. Chem. Phys.*, 2002, **4**, 1542–1548.

40 (*a*) M. Andruh, E. Bakalbassis, O. Kahn, J. C. Trombe and P. Porcher, Structure, spectroscopic and magnetic properties of rare earth metal(III) derivatives with the 2-formyl-4-methyl-6-(N-(2-pyridylethyl)formimidoyl)phenol ligand, *Inorg. Chem.*, 1993, **32**, 1616–1622; (*b*) O. Kahn, *Molecular Magnetism*, VHC Publishers, Inc., USA, 1993.

41 A. Zabala-Lekuona, J. M. Seco and E. Colacio, Single-Molecule Magnets: From Mn12-ac to dysprosium metallocenes, a travel in time, *Coord. Chem. Rev.*, 2021, **441**, 213984.

42 (*a*) K. N. Shrivastava, Theory of Spin–Lattice Relaxation, *Phys. Status Solidi B*, 1983, **117**, 437–458; (*b*) R. Orbach, On the theory of spin-lattice relaxation in paramagnetic salts, *Proc. Phys. Soc.*, 1961, **77**, 821–826; (*c*) H. B. G. Casimir and F. K. Du Pré, Note on the thermodynamic interpretation of paramagnetic relaxation phenomena, *Physica*, 1938, **5**, 507–511.

43 Y.-N. Guo, G.-F. Xu, Y. Guo and J. Tang, Relaxation dynamics of dysprosium(III) single molecule magnets, *Dalton Trans.*, 2011, **40**, 9953–9963.

44 N. F. Chilton, CC-FIT, program, **https://www.nfchilton.com/software.html**, 2014.

45 (*a*) P. P. Cen, S. Zhang, X. Y. Liu, W. M. Song, Y. Q. Zhang, G. Xie and S. P. Chen, Electrostatic potential determined magnetic dynamics observed in two mononuclear β-diketone dysprosium(III) single-molecule magnets, *Inorg. Chem.*, 2017, **56**, 3644–3656; (*b*) Z. G. Wang, J. Lu, C. Y. Gao, C. Wang, J. L. Tian, W. Gu, X. Liu and S. P. Yan, Single-ion magnet behavior of a new mononuclear dysprosium complex, *Inorg. Chem. Commun.*, 2013, **27**, 127–130; (*c*) X. L. Li, A. Wang, M. Cui, C. Gao, X. Yu, B. Su, L. Zhou, C. M. Liu, H. P. Xiao and Y. Q. Zhang, Modulating Two Pairs of Chiral DyIII Enantiomers by Distinct β-Diketone Ligands to Show Giant Differences in Single-Ion Magnet Performance and Nonlinear Optical Response, *Inorg. Chem.*, 2022, **61**, 9283–9294; (*d*) X. L. Li, C. Zhu, Q. Rong, J. Wei, R. Li, C. M. Liu, X.-L. Li, C. Zhu, Q. Rong, J. Wei, R. Li and C.-M. Liu, A pair of mononuclear Dy(III) enantiomers showing single-ion magnetic and ferroelectric properties, *New J. Chem.*, 2018, **42**, 10906–10911.

46 N. F. Chilton, D. Collison, E. J. L. McInnes, R. E. P. Winpenny and A. Soncini, An electrostatic model for the determination of magnetic anisotropy in dysprosium complexes, *Nat. Commun.*, 2013, **4**, 2551, DOI: **10.1038/ncomms3551**.

47 S. Kapurwan, A. Mondal, P. K. Sahu and S. Konar, *Inorg. Chem.*, 2022, **61**(44), 17459–17468.

48 (*a*) F. Guégan, J. Jung, B. L. Guennic, F. Riobé, O. Maury, B. Gillon, J. F. Jacquot, Y. Guyot, C. Morell and D. Luneau, Evidencing under-barrier phenomena in a Yb(III) SMM: a joint luminescence/neutron diffraction/SQUID study, *Inorg. Chem. Front.*, 2019, **6**, 3152–3157; (*b*) K. S. Pedersen, J. Dreiser, H. Weihe, R. Sibille, H. V. Johannesen, M. A. Sørensen, B. E. Nielsen, M. Sigrist, H. Mutka, S. Rols, J. Bendix and S. Piligkos, Design of Single-Molecule Magnets: Insufficiency of the Anisotropy Barrier as the Sole Criterion, *Inorg. Chem.*, 2015, **54**, 7600–7606; (*c*) D. Q. Wu, D. Shao, X. Q. Wei, F. X. Shen, L. Shi, Y. Q. Zhang and X. Y. Wang, Single-ion magnetism in seven-coordinate YbIII

complexes with distorted D5h coordination geometry, *Dalton Trans.*, 2017, **46**, 12884–12892; (*d*) W. Zhao, H. Cui, X.-Y. Chen, G. Yi, L. Chen, A. Yuan and C. L. Luo, An eight-coordinate ytterbium complex with a hexagonal bipyramid geometry exhibiting fieldinduced single-ion magnet behaviour, *Dalton Trans.*, 2019, **48**, 5621–5626.

49 (*a*) G. Cucinotta and J. Luzón, Magnetic anisotropy in a dysprosium/DOTA single-molecule magnet: Beyond simple magneto-structural correlations, *Angew. Chem., Int. Ed.*, 2012, **51**, 1606–1610; (*b*) D. Errulat, R. Marin, D. A. Gálico, K. L. M. Harriman, A. Pialat, B. Gabidullin, F. Iikawa, O. D. D. Couto Jr., J. O. Moilanen, E. Hemmer, F. A. Sigoli and M. Mugurescu, A Luminescent Thermometer Exhibiting Slow Relaxation of the Magnetization: Toward Self-Monitored Building Blocks for Next-Generation Optomagnetic Devices, *ACS Cent. Sci.*, 2019, **5**, 1187–1198; (*c*) J. Long, J. Rouquette, J.-M. Thibaud, R. A. S. Ferreira, L. D. Carlos, B. Donnadieu, V. Vieru, L. F. Chibotaru, L. Konczewicz, J. Haines, Y. Guari and J. Larionova, A High-Temperature Molecular Ferroelectric Zn/Dy Complex Exhibiting Single-Ion-Magnet Behavior and Lanthanide Luminescence, *Angew. Chem., Int. Ed.*, 2015, **54**, 2236–2240; (*d*) Y. Bi, C. Chen, Y.-F. Zhao, Y.-Q. Zhang, S.-D. Jiang, B.-W. Wang, J.-B. Han, J.-L. Sun, Z.-Q. Bian, Z.-M. Wanga and S. Gao, Thermostability and photoluminescence of Dy(III) single-molecule magnets under a magnetic field, *Chem. Sci.*, 2016, **7**, 5020–5031.

